Performance Analysis and Deep Learning Assessment of Full-Duplex Overlay Cognitive Radio NOMA Networks under Non-Ideal System Imperfections

Chandan Kumar Singh, *Student Member, IEEE*, Prabhat Kumar Upadhyay, *Senior Member, IEEE*, and Janne Lehtomäki, *Member, IEEE*

***Abstract*—In this paper, we investigate the effectiveness of an overlay cognitive radio (OCR) coupled with non-orthogonal multiple access (NOMA) system using a full-duplex (FD) cooperative spectrum access with a maximal ratio combining (MRC) scheme under the various non-ideal system imperfections. In view of practical realization, we ponder the impact of loop self-interference, transceiver hardware impairments, imperfect successive interference cancellation, and channel estimation errors on the system performance. We investigate the performance of the proposed system by obtaining closed-form expressions for outage probability and ergodic rate for primary as well as secondary users using Nakagami-*m* fading channels. As a result, we reveal some notable ceiling effects and present efficacious power allocation strategy for cooperative spectrum access. We further evaluate the system throughput and ergodic sum-rate (ESR) to assess the system's overall performance. Our findings manifest that the FD-based OCR-NOMA can comply with the non-ideal system imperfections and outperform the competing half-duplex (HD) and orthogonal multiple access (OMA) counterparts. Due to the massive complexity of the suggested system model, direct derivation of the closed-form formula for the ESR becomes cumbersome. To address this problem, we develop a deep neural network (DNN) framework for ESR prediction in real-time situations.**

***Index Terms*—Cognitive radio (CR), deep learning (DL), deep neural network (DNN), full-duplex (FD), hardware impairments (HIs), non-orthogonal multiple access (NOMA), overlay system.**

I. Introduction

In recent decades, the demand for high data rates has exploded. This significant increase in mobile data traffic should be matched by an increase in network spectral efficiency (SE) [1]. Non-orthogonal multiple access (NOMA) has emerged as the most promising technique to achieve this goal. It has been identified as a viable multiple access contender for next-generation communication systems because of its demonstrable superiority in enhancing SE and connection density with numerous users serviced on the same physical resource [2]. It serves multiple users by superimposing their signals in power domain over the same time/frequency resource at the transmitter side and detecting them through the process of successive interference cancellation (SIC) at the receiver side. As such, NOMA can enhance spectral and energy efficiencies and also provide huge connectivity and minimal transmission latency when compared to traditional orthogonal multiple access (OMA) [3]. However, NOMA methodologies may provide lower reliability of the network than traditional OMA methodologies due to interference from power-domain multiplexing.

Alternatively, the cognitive radio (CR) approach was developed to deal with the fast growing number of mobile applications under the limited spectrum resources [4]. Unlicensed secondary user (SU) can access spectrum that is only available to licensed primary user (PU) via the CR method, without interfering with the primary network [5]. CR may significantly improve the SE of wireless networks using three spectrum access paradigms: underlay, overlay, and interweave. The SU uses the interweave technique to strategically access licensed spectrum while depending on spectrum sensing [6] to detect PU activity. On the other hand, as long as the PU's quality-of-service (QoS) criterion is met, the overlay and underlay CR models allow PU and SU data to be transmitted in the same frequency band at the same time. With an underlay technique [7], SU can transfer data to its destination, subject to the interference temperature constraint imposed by the PU receiver. In contrast, in an overlay paradigm, the SU priorities aid the communication of PU by cooperating on a relay in exchange for access to the licensed spectrum of the PU [8].

A. Literature Review

In literature, the cognitive radio NOMA (CR-NOMA) refers to integrating NOMA into CR networks. It has proven to be a credible approach for enhancing the SE and reliability performance [9]. Till now, several studies have looked into CR-NOMA systems employing the underlay and overlay models. The outage probability (OP) performance and ergodic sum-rate (ESR) measurements of underlay CR-NOMA system utilizing decode-and-forward (DF) relaying protocols were investigated in [10], [11]. Unlike the underlay CR-NOMA model, an overlay CR-NOMA (OCR-NOMA) model employs a secondary transmitter (ST) as a PU relay, allowing it to communicate with the secondary receiver (SR) using the NOMA principle [12]. It is worth noting that in the OCR-NOMA system, the

This work is carried out under the Nokia Foundation Visiting Professor Grant and Visvesvaraya PhD Scheme of Ministry of Electronics & Information Technology (MeitY), Government of India, being implemented by Digital India Corporation (formerly Media Lab Asia). The work of J. Lehtomäki is supported in part by the Academy of Finland 6Genesis Flagship under Grant 318927.

C. K. Singh is with the Department of Electrical Engineering, Indian Institute of Technology Indore, Madhya Pradesh, India 453552 (e-mails: phd1801202003@iiti.ac.in).

P. K. Upadhyay is with the Department of Electrical Engineering, Indian Institute of Technology Indore, Madhya Pradesh, India 453552 and with the Centre for Wireless Communications (CWC), University of Oulu, 90014 Oulu, Finland (e-mails: pkupadhyay@iiti.ac.in).

J. Lehtomäki is with the Centre for Wireless Communications (CWC), University of Oulu, 90014 Oulu, Finland (e-mails: janne.lehtomaki@oulu.fi).

interference thermal barrier between the ST and the primary receiver (PR) could be removed, and additionally, PU's OP performance can be increased by utilizing the ST's relay cooperation diversity advantage [13]. However, because of the additional time resources required in a half-duplex (HD) relay cooperation mode, the OP performance enhancement in the aforementioned works comes at the cost of spectrum efficiency degradation [14]. Cooperative NOMA can improve performance benefits for remote users, but it also increases the system's bandwidth expenses. Adopting full-duplex (FD) relay technology is one viable option to get around this problem. Due to the fact that FD relays simultaneously receive and transmit data in the same frequency range, they have drawn a lot of attention from researchers who are working to develop more spectrally efficient systems. The NOMA system's throughput and outage performance were examined using FD cooperative relaying with a base energy harvesting in [15]. As reported in [16], FD cooperative spectrum sharing with NOMA support can be achieved by using the secondary receiver to assist the primary network in relaying information to the cell-edge primary user. A FD relay can be utilized to double the SE and improve the throughput of OCR-NOMA networks by allowing simultaneous transmission and reception over the same frequency channel [17]. The FD systems, on the other hand, suffer from residual loop self-interference (LI), which is caused by the FD transmitter towards its receiver. Although the LI can be reduced by using digital/analog cancellation and antenna design techniques [18], [19], but because of inadequate self-interference cancellation during decoding the intended signal, it still resides in the FD receiver. One intriguing technology for the future sixth-generation (6G) communication network is intelligent reflecting surface (IRS), which has the potential to intelligently increase the sum throughput of Internet-of-Things (IoT). Authors in [20] examined an IRS wireless-powered NOMA IoT network, where numerous NOMA IoT devices can connect with an access point (AP) using IRS. The performance of NOMA networks supporting ultra-reliable low-latency communications has been examined in [21] using the simultaneously transmitting and reflecting reconfigurable intelligent surface (STAR-RIS) technology.

Deep learning (DL) techniques have recently been identified as effective tools for addressing a variety of practical issues in current wireless communication networks, such as congestion control, resource allocation, and queue management [22]. A deep neural network (DNN) was exploited in [23] for wireless powered CR-NOMA-based IoT relay networks to enhance the productivity of a cell-edge user under perfect SIC (P-SIC) and imperfect SIC (I-SIC). In [24], DNN was built to solve classification and regression problems in cognitive two-way relaying networks for relay selection. G. Gui *et al*. [25] examined a DNN integrated into a NOMA system, and its great performance in terms of channel encoding, decoding, and detection has been confirmed.

B. Research Gap and Contributions

Despite the fact that there is significant participation in FD/HD CR-NOMA relaying transmission, it is still uncertain if such systems can achieve higher SE than primary direct link transmission (PDLT), particularly when mutual interference and QoS limitations are present. The performance of an FD-based OCR-NOMA system with PDLT using maximal ratio combining (MRC) at both primary and secondary users have yet to be studied theoretically. Furthermore, the adoption of FD relaying can improve the CR-NOMA system's SE, the existence of LI lowers the effective signal-to-interference plus noise ratio (SINR), forcing a trade-off between SE gain and system performance loss. In addition, due to in-quadrature-phase (I/Q) imbalances, amplifier non-linearities, and phase noises, radio-frequency (RF) transceivers are affected with hardware impairments (HIs) [26], [27]. Though various compensatory algorithms can reduce HIs, some residual impairments will always be present in practice [28]. Moreover, most of the preceding works presuppose perfect channel state information (CSI) at the receiver, which is too unrealistic for a practical system. In fact, receivers do not have access to precise CSI information, resulting in channel estimation errors (CEEs) which pose a substantial negative impact on the system's performance [29], [30]. It is worth noting that residual HIs and CEEs, as well as I-SIC [31], [32] in NOMA, may limit the capacity of the FD-based CR-NOMA system. Despite the fact that authors in [8], [12] looked at an HD-based NOMA in overlay spectrum sharing networks, they have, however, assumed ideal conditions such as P-SIC and perfect hardware in equipment, and without using a PDLT-link, examined the performance over simple Rayleigh fading channels. Whereas, in [7] and [33], authors worked on underlay spectrum sharing networks and considered the impact of I-SIC, but they assumed perfect hardware cases and do not exploit the PDLT-link, while assessing the results using Rayleigh and Nakagami-m fading channels, respectively. Authors in [30] considered the impact of CEEs on underlay spectrum sharing networks, but assumed a P-SIC and considered an HD relaying. To the best of the authors' knowledge, no previous research has examined the performance of FD-based OCR-NOMA systems under the joint impacts of non-ideal system imperfections such as I-SIC, CEEs, and HIs. It is worth mentioning that this type of analysis is necessary to understand the impact of non-ideal system imperfections on the practical design of CR-NOMA networks in order to create more sustainable and spectral-efficient wireless networks.

In light of the foregoing discussion, we propose an FD-based OCR-NOMA system with PDLT using MRC at both primary and secondary users for futuristic wireless communication networks. We consider the effects of non-ideal system imperfections such as LI in FD operation, I-SIC, CEEs, and HIs in the OCR-NOMA system for practical applications in 5G and beyond 5G contexts. It is probable that due to the degree of high complexity and variability of future wireless network service requirements such as OCR-NOMA. Traditional model-based approaches, i.e., through taking closed-form expressions, are no longer sufficient for deployment, network resource management, and operation. It is worth noting that with the advent of data-driven methods for evaluating system performance, such as DL modeling, precise and effective performance analysis is now possible without the need for the mathematical derivations that model-based methods require. Additionally,

data-driven approaches can be used to provide real-time setups, which is in line with the tendencies of future wireless systems. The limitation of the model-based approaches can therefore be overcome by the DL model for system metric evaluation. The following are the main contributions of the paper:

- We propose a cooperative spectrum access transmission (CSAT) approach for OCR-NOMA system that employs an FD-based DF relaying strategy in combination with PDLT. The PDLT alone scheme is also discussed as a benchmark for comparing the FD-based CSAT scheme performance for the OCR-NOMA system. In addition, we compare the performance of FD-based CSAT scheme to its HD and OMA counterparts to explore the physical layer design aspects.
- For the FD-based CSAT scheme across the Nakagami-m fading scenarios, we investigate the accurate and asymptotic OP performance and ergodic rate of the primary and secondary networks under non-ideal system imperfections. We further evaluate the system throughput and ESR to assess the overall performance of the FD OCR-NOMA system.
- We show how significant ceiling effects like the FD relay ceiling (FRC), secondary network ceiling (SNC), and entire system ceiling (ESC) affect the performance of the FD OCR-NOMA system. We also give an overview of the OCR-NOMA power allocation factor, which can be used to construct a future wireless network based on the FD OCR-NOMA model. Our findings show that the FD-based CSAT scheme can adjust for the effects of HIs and outperforms the competing HD and OMA-based CSAT schemes in the low signal-to-noise ratio (SNR) region.
- Because of their complex derivations, most earlier studies have not looked into the ESR for FD OCR-NOMA systems. This poses a significant barrier to the model-based method; and hence, we develop DNN model as a novel data-driven alternative for ESR prediction with high accuracy and low latency, with the goal of achieving practical real-time OCR-NOMA network configurations. In terms of anticipating the performance of complex network situations, the execution time and root-mean-square error (RMSE) are the major parameters for assessing the efficiency and accuracy of our design approach.

C. Organization

The remaining sections of this paper can be organized as follows. The system, channel and signal models for the OCR-NOMA using CSAT scheme are illustrated in Section II. In Section III, we present the OP performance analysis of primary network using an FD-based CSAT scheme and a PDLT alone scheme. Section IV examines the OP performance of the secondary network and overall system throughput. In Section V, we examine the ergodic rate and ESR performance of the system. The DNN framework design is presented in Section VI. In Section VII, the numerical and simulation findings are presented. Finally, Section VIII brings the conclusion of the work. Furthermore, proofs of useful theorems are consigned to the appendices.

Mathematical Functions and Notations: The cumulative distribution function (CDF) and probability density function (PDF) of a random variable X are represented by $F_X(\cdot)$ and $f_X(\cdot)$, respectively. A complex Gaussian distribution with mean zero and variance σ^2 is denoted as $\mathcal{CN}(0,\sigma^2)$. Expectation is denoted by $\mathbb{E}[\cdot]$, and probability is denoted by $\mathbb{P}_r[\cdot]$. $\binom{p}{q}$ represents the binomial coefficient. Furthermore, $\mathcal{K}_v(\cdot)$ is the second-kind modified Bessel function [34, eq. 8.432.6], whereas $\Gamma(\cdot)$ and $\Upsilon(\cdot,\cdot)$ are the complete and lower incomplete Gamma functions, respectively, as provided in [34, eqs. (8.310.1) and (8.350.1)].

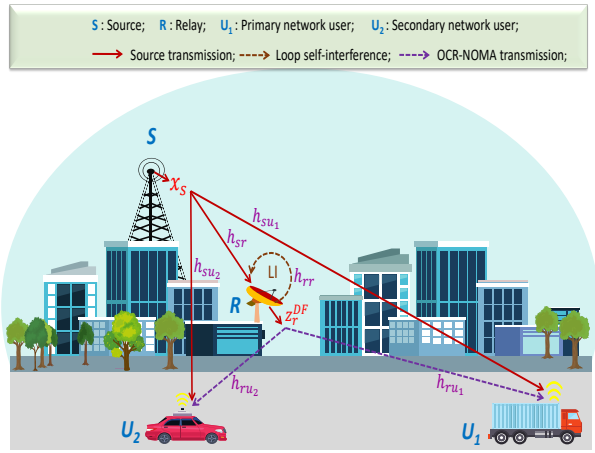

Fig. 1: FD-based OCR-NOMA system model.

II. System Description and CSAT Scheme

This section describes the proposed OCR-NOMA system using CSAT scheme under the relevant channel model, followed by the SINR expressions at the receiving nodes.

A. System Model

As shown in Fig. 1, we consider an FD-based CSAT scheme for the OCR-NOMA system, wherein a primary network having a source (S)–user (U_1) pair coexists with a secondary network having source (R)–user (U_2) pair. Despite the fact that between the primary source S and its user U_1, a direct transmission (DT) link exists, S takes advantage of diversity by using a CSAT link with the help of node R. The node R serves as a cooperative DF relay for transmission of primary source's data to user U_1, and in exchange, it receives primary spectrum access for its own data transfer to user U_2. Based upon the OCR-NOMA principle, R splits available power to transmit simultaneously primary source's data to user U_1 and its own data to user U_2. Additionally, R uses two distinct antennas to work on FD mode [35], and thereby, it can simultaneously transmit and receive signals. Whereas, all other nodes are assumed to be equipped with single antenna[1] to work on HD mode [14]. Despite the fact that several approaches for minimizing LI effects in FD systems have been developed [19], LI will continue to affect the relay node, which is proportionate to the transmit power used at the FD relay node [17]. Other than this, devices are affected by HIs due to the use of

[1]Sensors or other devices in future enormous machine-type communication networks are typically supplied with a single antenna for applications that merge IoT with cellular networks.

less expensive components at the RF transceiver section, and hence transceivers are affected by the distortion noises. We also assume that the additive white Gaussian noise (AWGN), modelled as $\mathcal{CN}(0,\sigma^2)$, makes an impact on each receiving node.

B. Channel Model

We assume that each channel has block fading, which means that it stays constant during the current block transmission but it may change in the next. The channel coefficients for the particular channels $S \to U_1$, $S \to R$, $S \to U_2$, $R \to R$, $R \to U_1$, and $R \to U_2$ are represented by h_{su_1}, h_{sr}, h_{su_2}, h_{rr}, h_{ru_1}, and h_{ru_2}, respectively. We further assume that the channel coefficients h_{ij} are distributed according to independent Nakagami-*m* fading[2], where $i \in \{s,r\}$, $j \in \{u_1,r,u_2\}$, and $i \neq j$. As a result, the channel gain $|h_{ij}|^2$ follows a gamma distribution with the respective CDF and PDF as

$$F_{|h_{ij}|^2}(v) = \frac{1}{\Gamma(m_{ij})}\Upsilon\left(m_{ij}, \frac{m_{ij}}{\Omega_{ij}}v\right), \tag{1}$$

and

$$f_{|h_{ij}|^2}(v) = \left(\frac{m_{ij}}{\Omega_{ij}}\right)^{m_{ij}} \frac{1}{\Gamma(m_{ij})}\, v^{m_{ij}-1}\, \mathrm{e}^{-\frac{m_{ij}}{\Omega_{ij}}v}, \tag{2}$$

with m_{ij} representing fading severity parameter and Ω_{ij} representing average fading power. We also assume that the LI fading channel coefficient h_{rr} follows Nakagami-*m* distribution [29] with average LI power $\mathbb{E}[|h_{rr}|^2] = k_r\Omega_{rr}$, where k_r ($0 \leq k_r \leq 1$) represents the level of LI cancellation, i.e., $k_r = 0$ indicates that LI is absent in the system. We exploit the linear minimum mean square error (LMMSE) channel estimation model. Under CEEs [29], $h_{ij} = \hat{h}_{ij} + e_{ij}$, where $i \in \{s,r\}$, $j \in \{u_1,u_2\}$, and $i \neq j$, and $\hat{h}_{ij}$ and e_{ij} represent the estimated channel coefficient and estimation error, respectively. Hereby, $\hat{h}_{ij}$ follows the Nakagami-*m* distribution with fading severity parameter $\hat{m}_{ij}$ and average fading power $\mathbb{E}[|\hat{h}_{ij}|^2] = \hat{\Omega}_{ij}$. Further, the estimation error e_{ij} follows $\mathcal{CN}(0,\epsilon_{ij}^2)$ [29]. Assuming $|\hat{h}_{ij}|^2$ and $|e_{ij}|^2$ are mutually independent and orthogonal, $\mathbb{E}[|\hat{h}_{ij}|^2] = \mathbb{E}[|h_{ij}|^2] - \mathbb{E}[|e_{ij}|^2]$. As we know that $\mathbb{E}[|h_{ij}|^2] = \Omega_{ij}$, therefore $\mathbb{E}[|\hat{h}_{ij}|^2] = \Omega_{ij} - \epsilon_{ij}^2$.

C. Signal Model

The primary source S transmits its unit-power signal $x_s(t)$ to U_1 which is also reached to R and U_2. As a result, the received signals through DT links at the end users U_1 and U_2 can be expressed at time t as

$$y_{sj}(t) = (\hat{h}_{sj} + e_{sj})\big(\sqrt{P_s}\, x_s(t) + n_{sj}(t)\big) + \psi_{sj}(t), \tag{3}$$

where $j \in \{u_1,u_2\}$, P_s is the transmit power at S, $n_{sj}(t) \sim \mathcal{CN}(0,\theta_{sj}^2 P_s)$ represents the distortion noise from aggregated transceiver impairments at j^{th} node, and $\psi_{sj}(t)$ is the AWGN. Herein, θ_{sj} represents the aggregated level of HIs at transceivers [30] such that $\theta_{sj} = \sqrt{\theta_{ts}^2 + \theta_{rsj}^2}$, where θ_{ts} and θ_{rsj} being the level of HIs at transmit and receive processing, respectively, which can be quantified as an error vector magnitudes (EVMs)[3] by experiment. Therefore, the resultant signal-to-noise-and-distortion ratio (SNDR) at j^{th} node, $j \in \{u_1,u_2\}$, through the DT-link can be obtained as

$$\gamma_{sj}^{\mathrm{DT}} = \frac{\Delta_s\,|\hat{h}_{sj}|^2}{\Delta_s\,|\hat{h}_{sj}|^2\theta_{sj}^2 + \phi_{sj}}, \tag{4}$$

where $\Delta_s = \frac{P_s}{\sigma^2}$ be the transmit SNR and $\phi_{sj} = \Delta_s\,\epsilon_{sj}^2\,(1+\theta_{sj}^2)+1$. While, as R operates in FD mode, the LI signal causes residual interference. Hence, the received signal at R is given as

$$y_{sr}(t) = \big(\hat{h}_{sr} + e_{sr}\big)\big(\sqrt{P_s}\, x_s(t) + n_{sr}(t)\big) + \underbrace{h_{rr}\big(z_r^{\mathrm{DF}}(t-\tau) + n_{rr}(t-\tau)\big)}_{\text{Loop self-interference term}} + \psi_{sr}(t), \tag{5}$$

where $z_r^{\mathrm{DF}}(t-\tau)$ is the LI signal with $\mathbb{E}[|z_r^{\mathrm{DF}}(t-\tau)|^2] = P_r$, P_r be the transmit power at R, $n_{sr}(t) \sim \mathcal{CN}(0,\theta_{sr}^2 P_s)$ and $n_{rr}(t-\tau) \sim \mathcal{CN}(0,\theta_{rr}^2 P_r)$ represent the distortion noises from aggregated transceiver impairments at the relay, where θ_{sr} and θ_{rr} being the aggregated level of HIs at transceivers, τ denotes the processing delay, and $\psi_{sr}(t)$ is the AWGN. Here, we have $\theta_{sr} = \sqrt{\theta_{ts}^2 + \theta_{rsr}^2}$ and $\theta_{rr} = \sqrt{\theta_{tr}^2 + \theta_{rrr}^2}$, with θ_{ts} or θ_{tr} and θ_{rsr} or θ_{rrr} denoting the transmitter and receiver HIs levels, respectively. Thus, the SNDR at R via the DT-link can be given as

$$\gamma_{sr}^{\mathrm{DT}} = \frac{\Delta_s\,|\hat{h}_{sr}|^2}{\Delta_s\,|\hat{h}_{sr}|^2\theta_{sr}^2 + \Delta_r|h_{rr}|^2(1+\theta_{rr}^2) + \phi_{sr}}, \tag{6}$$

where $\Delta_r = \frac{P_r}{\sigma^2}$ and $\phi_{sr} = \Delta_s\,\epsilon_{sr}^2\,(1+\theta_{sr}^2) + 1$.

As the node R facilitates DF-based relaying cooperation, it executes the decoding of the source signal $x_s(t)$. If decoding is successful, the relay merges the decoded signal $x_s(t)$ with its own signal $x_r(t)$ using NOMA principle to transmit a superimposed signal $z_r^{\mathrm{DF}}(t) = \sqrt{\delta_1\,P_r}\,x_s(t) + \sqrt{\delta_2\,P_r}\,x_r(t)$, where the factors δ_1 and δ_2 signify the power allocation parameters such that $\sum_{j=1}^{2}\delta_j = 1$. Considering the typical scenario under overlay spectrum sharing (IoT or D2D-based secondary networks), it is assumed that, the distance between R and U_1 is greater than the distance between R and U_2, i.e., $d_{ru_1} \geq d_{ru_2}$. Moreover, in anticipation to the higher priority of PU, we consider $\delta_1 > \delta_2$, i.e., a greater power is allocated to primary communication than secondary communication [7], [29]. As such, the relay's transmit power allocation for U_2 will be dependent on satisfying the QoS constraint at U_1 in terms of OP, as discussed later in Section III-D. The acquired signals at U_1 and U_2 from R can be given by

$$y_{rj}^{\mathrm{DF}}(t) = (\hat{h}_{rj} + e_{rj})\big(z_r^{\mathrm{DF}}(t) + n_{rj}(t)\big) + \psi_{rj}(t), \tag{7}$$

where $j \in \{u_1,u_2\}$, $n_{rj}(t) \sim \mathcal{CN}(0,\theta_{rj}^2 P_r)$ represents the distortion noise from aggregated transceiver impairments, and $\psi_{rj}(t)$ is the AWGN. Herein, $\theta_{rj} = \sqrt{\theta_{tr}^2 + \theta_{rrj}^2}$ is the aggregated level of HIs at transceivers, with θ_{tr} be the HIs at transmit and θ_{rrj} be the HIs at receive processing. Consequently, the SNDR at U_1 can be expressed via the relay link as

[2]The Nakagami-*m* fading model is a generalised model that encompasses a number of fading scenarios for terrestrial wireless channels, including the well-known Rayleigh fading as a special case (with $m = 1$) [14]. Furthermore, Nakagami-*m* fading is more accurate than Rayleigh fading in terms of matching experimentally collected measurement data.

[3]The ratio of the average distortion magnitude to the average signal magnitude is the EVM, which is a typical quality measure of RF transceivers. The more precise and costlier transceiver hardware is represented by the smaller EVMs [36], [37].

$$\gamma_{ru_1}^{\text{DF}} = \frac{\delta_1\,\Delta_r\,|\hat{h}_{ru_1}|^2}{\Delta_r\,\lambda_p\,|\hat{h}_{ru_1}|^2 + \phi_{ru_1}}, \tag{8}$$

where $\lambda_p = \delta_2 + \theta_{ru_1}^2$ and $\phi_{ru_1} = \Delta_r\,\epsilon_{ru_1}^2\,(1+\theta_{ru_1}^2)+1$. As the signals from S and R have some time delay, U_1 is considered to be capable of fully resolving these signals, so that they can be properly co-phased and merged using the MRC [38]. As a result, the SNDR after MRC at node U_1 can be expressed as $\gamma_{u_1}^{\text{MRC}} = \gamma_{su_1}^{\text{DT}} + \gamma_{ru_1}^{\text{DF}}$.

On the other hand, the U_2 carries out SIC according to the NOMA principle. For this, U_2 first decodes the primary source's signal while treating the relay's signal as a noise. Thus, the resultant SNDR expression at U_2 to decode $x_s(t)$ can be expressed as

$$\gamma_{ru_2,x_s}^{\text{DF}} = \frac{\delta_1\,\Delta_r\,|\hat{h}_{ru_2}|^2}{\Delta_r\,\lambda_s\,|\hat{h}_{ru_2}|^2 + \phi_{ru_2}}, \tag{9}$$

where $\lambda_s = \delta_2 + \theta_{ru_2}^2$ and $\phi_{ru_2} = \Delta_r\,\epsilon_{ru_2}^2\,(1+\theta_{ru_2}^2)+1$. Noting that $x_s(t)$ has also been received at U_2 from source S, the U_2 employs MRC to combine the primary signals received through DT and relay links. Therefore, we have $\gamma_{u_2}^{\text{MRC}} = \gamma_{su_2}^{\text{DT}} + \gamma_{ru_2,x_s}^{\text{DF}}$. Afterwards, U_2 decodes its own signal $x_r(t)$ by removing $x_s(t)$ from $y_{ru_2}^{\text{DF}}(t)$. Thereby, the SNDR at U_2 is given as

$$\gamma_{ru_2}^{\text{DF}} = \frac{\delta_2\,\Delta_r\,|\hat{h}_{ru_2}|^2}{\Delta_r\,|\hat{h}_{ru_2}|^2\,\theta_{ru_2}^2 + \delta_1\,\Delta_r\,|h_{u_2}|^2 + \phi_{ru_2}}, \tag{10}$$

where h_{u_2} is the residual interference signal (IS) [39] channel coefficient at U_2 and is subject to Nakagami-*m* fading with fading severity m_{u_2} and average power $\mathbb{E}[|h_{u_2}|^2] = k_2\Omega_{u_2}$. Herein, k_2 ($0 \le k_2 \le 1$) accounts for the level of residual IS due to I-SIC, i.e., $k_2 = 0$ implies the case of P-SIC.

On the contrary, if the relay is unable to decode $x_s(t)$, then the relay will be in a silent state. In this case, U_1 receives $x_s(t)$ only from the source S through the DT-link.

III. Performance Analysis of Primary Network

In this section, we analyze the accurate and asymptotic OP performance of the primary network employing CSAT scheme and compare its performance with a baseline PDLT alone scheme. Eventually, we uncover significant ceiling effects relating to the HIs and examine the NOMA-based CSAT power allocation policy.

A. Accurate OP Analysis:

Primary network's OP can be deduced for a target rate r_{th}^p as

$$\begin{aligned}\mathcal{P}_{\text{Pri}}^{\text{CSAT}}(r_{\text{th}}^p) &= \mathbb{P}_r\big[\gamma_{sr}^{\text{DT}} \ge \tau_p,\ \big(\gamma_{su_1}^{\text{DT}} + \gamma_{ru_1}^{\text{DF}}\big) < \tau_p\big] \\ &\quad + \mathbb{P}_r\big[\gamma_{sr}^{\text{DT}} < \tau_p, \gamma_{su_1}^{\text{DT}} < \tau_p\big],\end{aligned} \tag{11}$$

where $\tau_p = 2^{r_{\text{th}}^p} - 1$. In (11), the first term represents the probability that R can decode x_s successfully, while U_1 fails to decode x_s via MRC between the DT and relay links; and the second term denotes the probability that neither R nor U_1 can decode x_s. We can further evaluate (11) as

$$\begin{aligned}\mathcal{P}_{\text{Pri}}^{\text{CSAT}}(r_{\text{th}}^p) &= \big(1 - F_{\gamma_{sr}^{\text{DT}}}(\tau_p)\big)\underbrace{\mathbb{P}_r\big[\,\big(\gamma_{su_1}^{\text{DT}} + \gamma_{ru_1}^{\text{DF}}\big) < \tau_p\big]}_{\mathcal{P}_{u_1}} \\ &\quad + F_{\gamma_{sr}^{\text{DT}}}(\tau_p)\,F_{\gamma_{su_1}^{\text{DT}}}(\tau_p).\end{aligned} \tag{12}$$

To proceed, we first obtain the CDF $F_{\gamma_{su_1}^{\text{DT}}}(\tau_p)$ using (4) as

$$F_{\gamma_{su_1}^{\text{DT}}}(\tau_p) = \begin{cases} F_{|\hat{h}_{su_1}|^2}\left(\frac{\phi_{su_1}\tau_p}{\Delta_s(1-\theta_{su_1}^2\tau_p)}\right), & \text{if } \tau_p < \frac{1}{\theta_{su_1}^2}, \\ 1, & \text{if } \tau_p \ge \frac{1}{\theta_{su_1}^2}. \end{cases} \tag{13}$$

To assess (12), we first compute the expression of $F_{\gamma_{sr}^{\text{DT}}}(\tau_p)$ with the help of following theorem.

Theorem 1: The CDF $F_{\gamma_{sr}^{\text{DT}}}(\tau_p)$ for CSAT scheme is given by

$$F_{\gamma_{sr}^{\text{DT}}}(\tau_p) = \begin{cases} \Psi_1(\tau_p), & \text{if } \tau_p < \frac{1}{\theta_{sr}^2}, \\ 1, & \text{if } \tau_p \ge \frac{1}{\theta_{sr}^2}, \end{cases} \tag{14}$$

with

$$\begin{aligned}\Psi_1(\tau_p) &= 1 - \sum_{a=0}^{m_{sr}-1}\sum_{b=0}^{a}\frac{1}{a!}\left(\frac{m_{sr}\tau_p}{\hat{\Omega}_{sr}\Delta_s\vartheta}\right)^a\frac{1}{\Gamma(m_{rr})} \\ &\times\left(\frac{m_{rr}}{\Omega_{rr}\Delta_r}\right)^{m_{rr}}\binom{a}{b}(\phi_{sr})^{a-b}\big(1+\theta_{rr}^2\big)^b(b+m_{rr}-1)! \\ &\times\left(\frac{m_{sr}\tau_p(1+\theta_{rr}^2)}{\hat{\Omega}_{sr}\Delta_s\vartheta} + \frac{m_{rr}}{\Omega_{rr}\Delta_r}\right)^{-(b+m_{rr})} e^{-\left(\frac{m_{sr}\phi_{sr}\tau_p}{\hat{\Omega}_{sr}\Delta_s\vartheta}\right)},\end{aligned} \tag{15}$$

where $\vartheta = 1 - \theta_{sr}^2\,\tau_p$.

Proof: See Appendix A. ∎

Next, the evaluation of $\mathcal{P}_{u_1}$ in (12) can be carried out as

$$\mathcal{P}_{u_1} = \int_0^{\tau_p}\int_0^{\tau_p - y} f_{\gamma_{ru_1}^{\text{DF}}}(x)\,f_{\gamma_{su_1}^{\text{DT}}}(y)\,dx\,dy, \tag{16}$$

$$= \int_0^{\tau_p} F_{\gamma_{ru_1}^{\text{DF}}}(\tau_p - y) f_{\gamma_{su_1}^{\text{DT}}}(y)\,dy. \tag{17}$$

The computation of (17) requires the CDF $F_{\gamma_{ru_1}^{\text{DF}}}(\cdot)$ which can be deduced using (8) as

$$F_{\gamma_{ru_1}^{\text{DF}}}(\tau_p) = \begin{cases} F_{|\hat{h}_{ru_1}|^2}\left(\frac{\phi_{ru_1}\tau_p}{\Delta_r(\delta_1 - \lambda_p\tau_p)}\right), & \text{if } \tau_p < \frac{\delta_1}{\lambda_p}, \\ 1, & \text{if } \tau_p \ge \frac{\delta_1}{\lambda_p}. \end{cases} \tag{18}$$

Furthermore, it is realised that a closed-form solution for $\mathcal{P}_{u_1}$ would be intractable by employing the $F_{\gamma_{ru_1}^{\text{DF}}}(\cdot)$ expression from (18) and putting the PDF expression of $\gamma_{su_1}^{\text{DT}}$ into (17). As a result, for the convoluted integral sector in (16), we use an H-stairways conjecture [40] to simplify $\mathcal{P}_{u_1}$ as

$$\begin{aligned}\mathcal{P}_{u_1} &\approx \sum_{i=0}^{H-1}\left\{F_{\gamma_{su_1}^{\text{DT}}}\left(\frac{i+1}{H}\,\tau_p\right) - F_{\gamma_{su_1}^{\text{DT}}}\left(\frac{i}{H}\,\tau_p\right)\right\} \\ &\quad\times F_{\gamma_{ru_1}^{\text{DF}}}\left(\frac{H-i}{H}\,\tau_p\right).\end{aligned} \tag{19}$$

Finally, on inserting the CDF expressions from (13) and (18) into (19) and the result along with (13) and (14) into (12), $\mathcal{P}_{\text{Pri}}^{\text{CSAT}}(r_{\text{th}}^p)$ can be evaluated.

We also consider a baseline PDLT alone scheme that facilitates primary communication between S and U_1 through a DT link only i.e., no involvement of cooperative spectrum sharing through secondary node R. For this PDLT alone scheme, the OP is formulated as $\mathcal{P}_{\text{Pri}}^{\text{DT}}(r_{\text{th}}^p) = \mathbb{P}_r\left[\log_2\left(1+\gamma_{su_1}^{\text{DT}}\right) < r_{\text{th}}^p\right] = \mathbb{P}_r\left[\gamma_{su_1}^{\text{DT}} < \tau_p^{\text{DT}}\right] = F_{\gamma_{su_1}^{\text{DT}}}(\tau_p^{\text{DT}})$, where $\tau_p^{\text{DT}} = 2^{r_{\text{th}}^p} - 1$ is the predefined SNDR threshold for DT-link. One can evaluate this OP readily using (13).

B. Asymptotic OP Analysis

We obtain an asymptotic OP expression in (12) for high SNR ($\Delta_s, \Delta_r \to \infty$) to reveal the diversity order. First, making use of the fact that the lower incomplete gamma function $\Upsilon(m, z)$ [34, eq. 8.354.1] can be approximated as

$$\Upsilon(m,z)=\sum_{a=0}^{\infty}\frac{(-1)^a\,z^{m+a}}{a!\,(m+a)}\underset{z\to 0}{\approx}\left(\frac{z^m}{m}\right), \tag{20}$$

we can modify CDF from (1), at high SNR, as

$$F_{|h_{ij}|^2}(x)\approx\frac{1}{\Gamma(m_{ij}+1)}\left(\frac{m_{ij}}{\Omega_{ij}}x\right)^{m_{ij}}. \tag{21}$$

Therefore, the asymptotic OP for the PDLT scheme can be deduced as

$$\begin{aligned}\mathcal{P}_{\text{Pri}}^{\text{DT, asy}(\infty)}(r_{\text{th}}^p)&=F_{\gamma_{su_1}^{\text{DT}}}^{\text{asy}(\infty)}(\tau_p^{\text{DT}})\\&=\frac{1}{\Gamma(m_{su_1}+1)}\left(\frac{m_{su_1}}{\hat{\Omega}_{su_1}}\right)^{m_{su_1}}\left(\frac{\tau_p^{\text{DT}}\,\phi_{su_1}}{\Delta_s(1-\theta_{su_1}^2\tau_p^{\text{DT}})}\right)^{m_{su_1}}.\end{aligned} \tag{22}$$

We can further evaluate the asymptotic OP for the CSAT scheme for primary network as

$$\begin{aligned}\mathcal{P}_{\text{Pri}}^{\text{CSAT, asy}(\infty)}(r_{\text{th}}^p)&=\big(1-F_{\gamma_{sr}^{\text{DT}}}^{\text{asy}(\infty)}(\tau_p)\big)\underbrace{\mathbb{P}_r\big[\,\big(\gamma_{su_1}^{\text{DT}}+\gamma_{ru_1}^{\text{DF}}\big)<\tau_p\big]}_{\mathcal{P}_{u_1}^{\text{asy}(\infty)}}\\&\quad+F_{\gamma_{sr}^{\text{DT}}}^{\text{asy}(\infty)}(\tau_p)\;F_{\gamma_{su_1}^{\text{DT}}}^{\text{asy}(\infty)}(\tau_p).\end{aligned} \tag{23}$$

For the computation of (23), we calculate the asymptotic expressions of the involved CDFs and probability term as follows.

Lemma 1: The CDF $F_{\gamma_{sr}^{\text{DT}}}^{\text{asy}(\infty)}(\tau_p)$ for FD-based CSAT scheme can be expressed under Nakagami-m fading as

$$\begin{aligned}F_{\gamma_{sr}^{\text{DT}}}^{\text{asy}(\infty)}(\tau_p)&=\sum_{a=0}^{m_{sr}}\frac{1}{\Gamma(m_{sr}+1)}\left(\frac{m_{sr}}{\hat{\Omega}_{sr}}\right)^{m_{sr}}\left(\frac{\tau_p}{\Delta_s\vartheta}\right)^{m_{sr}}\binom{m_{sr}}{a}\\&\quad\times\big(\Delta_r(1+\theta_{rr}^2)\big)^a\;\big(\phi_{sr}\big)^{(m_{sr}-a)}\;\frac{1}{\Gamma(m_{rr})}\\&\quad\times\left(\frac{m_{rr}}{\Omega_{rr}}\right)^{m_{rr}}(m_{rr}-1+a)!\left(\frac{m_{rr}}{\Omega_{rr}}\right)^{-(m_{rr}+a)},\end{aligned} \tag{24}$$

for $\tau_p<\frac{1}{\theta_{sr}^2}$.

Proof: First, the related PDF expressions are inserted in (76), and the integral expression is then simplified using [34, eq. 3.351.1] and [34, eq. 1.111] while using series expansion of $\Upsilon(m,z)$ as given in (20). Lastly, solving the involved integral in (76) using (20), we obtain the desired expression of $F_{\gamma_{sr}^{\text{DT}}}^{\text{asy}(\infty)}(\tau_p)$ as in (24). ∎

Similar to condition like (18), the CDF $F_{\gamma_{ru_1}^{\text{DF}}}^{\text{asy}(\infty)}(\tau_p)$ can be calculated as

$$F_{\gamma_{ru_1}^{\text{DF}}}^{\text{asy}(\infty)}(\tau_p)=\frac{1}{\Gamma(m_{ru_1}+1)}\left(\frac{m_{ru_1}}{\hat{\Omega}_{ru_1}}\right)^{m_{ru_1}}\left(\frac{\tau_p\phi_{ru_1}}{\Delta_r(\delta_1-\lambda_p\tau_p)}\right)^{m_{ru_1}}, \tag{25}$$

for $\tau_p<\frac{\delta_1}{\lambda_p}$. Next, the evaluation of $\mathcal{P}_{u_1}^{\text{asy}(\infty)}$ in (23) can be carried out similar to condition like (19) as

$$\begin{aligned}\mathcal{P}_{u_1}^{\text{asy}(\infty)}&\approx\sum_{i=0}^{H-1}\left\{F_{\gamma_{su_1}^{\text{DT}}}^{\text{asy}(\infty)}\Big(\frac{i+1}{H}\,\tau_p\Big)-F_{\gamma_{su_1}^{\text{DT}}}^{\text{asy}(\infty)}\Big(\frac{i}{H}\,\tau_p\Big)\right\}\\&\quad\times F_{\gamma_{ru_1}^{\text{DF}}}^{\text{asy}(\infty)}\Big(\frac{H-i}{H}\,\tau_p\Big).\end{aligned} \tag{26}$$

Finally, on inserting the CDF expressions from (22) and (25) into (26) and the result along with (22) and (24) into (23), $\mathcal{P}_{\text{Pri}}^{\text{CSAT, asy}(\infty)}(r_{\text{th}}^p)$ can be evaluated. Thus, on applying [38] $d_{\text{Pri}}^{\text{DT}}=-\lim_{\Delta\to\infty}\frac{\log(\mathcal{P}_{\text{Pri}}^{\text{DT, asy}(\infty)}(\Delta))}{\log(\Delta)}$ and $d_{\text{Pri}}^{\text{CSAT}}=-\lim_{\Delta\to\infty}\frac{\log(\mathcal{P}_{\text{Pri}}^{\text{CSAT, asy}(\infty)}(\Delta))}{\log(\Delta)}$ with $\Delta\triangleq\Delta_s=\Delta_r$, the primary network's diversity orders for PDLT and CSAT schemes are $d_{\text{Pri}}^{\text{DT}}=0$ and $d_{\text{Pri}}^{\text{CSAT}}=0$, respectively. This is attributed to the impact of the non-ideal system imperfections. Hereby, we infer that error floors would result for the pertinent OP curves in the high SNR regime.

C. Ceiling Effects in Primary Network

The primary network of the proposed OCR-NOMA system suffers from two types of ceiling effects known as FRC and ESC that arise due to undesired constraints placed on τ_p under the HIs. When the relay cooperation in the FD OCR-NOMA system goes into outage due to undesirable limits imposed on the threshold τ_p, the FRC effect arises. From (14), it can be seen that, for $\tau_p\geq\frac{1}{\theta_{sr}^2}$, then the CDF $F_{\gamma_{sr}^{\text{DT}}}(\tau_p)$ reaches unity. Also from (18), we can see that, for $\tau_p\geq\frac{\delta_1}{\lambda_p}$, the CDF $F_{\gamma_{ru_1}^{\text{DF}}}(\tau_p)$ attains unity. As a result, the relay cooperation comes to a standstill. Consequently, the primary network's OP performance relies solely on the DT link. Further, from (13), when the τ_p reaches $\frac{1}{\theta_{su_1}^2}$, the DT link also goes into outage, and it is referred to as the ESC effect. For an acceptable range of system parameters, especially power allocation parameter δ_1, $\frac{\delta_1}{\lambda_p}$ is always less than $\frac{1}{\theta_{sr}^2}$ or $\frac{1}{\theta_{su_1}^2}$. It shows FRC occurs before the ESC.

D. NOMA-based CSAT Power Allocation Policy

In order to maintain the QoS for the primary network, we must choose a practical value for the NOMA-based CSAT power allocation parameter δ_1. As revealed in the previous subsection, we can fetch an allowable range of δ_1 for a predetermined threshold τ_p as $\frac{\tau_p(1+\theta_{ru_1}^2)}{1+\tau_p}<\delta_1<1$ under the proposed CSAT scheme. Furthermore, by satisfying the criterion $\mathcal{P}_{\text{Pri}}^{\text{CSAT}}(r_{\text{th}}^p)\leq\mathcal{P}_{\text{Pri}}^{\text{DT}}(r_{\text{th}}^p)$, the effective value of δ_1 for overlay spectrum sharing may be determined for a given target rate r_{th}^p. It is worth mentioning that a lower δ_1 value can supply more CSAT power to the secondary communication, resulting in more significant spectrum access opportunities.

IV. Performance Analysis of Secondary Network

We conduct hereby accurate and asymptotic OP analysis of the secondary network for the OCR-NOMA system under the FD CSAT scheme by considering the two SIC scenarios i.e., P-SIC and I-SIC. It additionally embellishes the secondary network's ceiling effects, power optimization for users' fairness, followed by throughput of the overall FD OCR-NOMA system.

A. Accurate OP Analysis

The OP for the secondary network under FD-based CSAT scheme can be expressed for a given target rate r_{th}^s as

$$\begin{aligned}\mathcal{P}_{\text{Sec}}^{\text{CSAT}}(r_{\text{th}}^s)&=\mathbb{P}_r\big[\gamma_{sr}^{\text{DT}}\geq\tau_p\big]\big(1-\underbrace{\mathbb{P}_r\big[\gamma_{u_2}^{\text{MRC}}\geq\tau_p,\,\gamma_{ru_2}^{\text{DF}}\geq\tau_s\big]}_{\mathcal{P}_{u_2}}\big)\\&\quad+\mathbb{P}_r\big[\gamma_{sr}^{\text{DT}}<\tau_p\big],\end{aligned} \tag{27}$$

where $\tau_s=2^{r_{\text{th}}^s}-1$. The first term in (27) represents the probability that U_2 will fail to decode either x_s or x_r, even if R successfully decodes x_s; and the second term represents the probability that R will fail to decode x_s, causing U_2 to remain silent. Hereby, (27) can be further evaluated as

$$\mathcal{P}_{\text{Sec}}^{\text{CSAT}}(r_{\text{th}}^s)=\big[1-F_{\gamma_{sr}^{\text{DT}}}(\tau_p)\big]\big(1-\mathcal{P}_{u_2}\big)+F_{\gamma_{sr}^{\text{DT}}}(\tau_p). \tag{28}$$

For the computation of (28), we require the expression for the joint probability term $\mathcal{P}_{u_2}$ which is derived in the succeeding subsections under I-SIC and P-SIC cases.

1) I-SIC: For the case of I-SIC, we derive the expression of $\mathcal{P}_{u_2}$ in the following theorem.

Theorem 2: The probability $\mathcal{P}_{u_2}$ in (28) can be evaluated as

$$\mathcal{P}_{u_2} = \begin{cases} \mathcal{P}_{u_{21}} \times \mathcal{P}_{u_{22}}, & \text{if } \tau_p > \frac{\delta_1}{\lambda_s}, \\ \mathcal{P}_{u_{22}}, & \text{if } \tau_p \leq \frac{\delta_1}{\lambda_s}, \end{cases} \tag{29}$$

with

$$\mathcal{P}_{u_{21}} \approx 1 - \sum_{i=0}^{H-1} \left\{ F_{\gamma_{su_2}^{\text{DT}}}\Big(\frac{i+1}{H}\,\tau_p\Big) - F_{\gamma_{su_2}^{\text{DT}}}\Big(\frac{i}{H}\,\tau_p\Big) \right\} \times F_{\gamma_{ru_2,x_s}^{\text{DF}}}\Big(\frac{H-i}{H}\,\tau_p\Big) \tag{30}$$

and

$$\mathcal{P}_{u_{22}} = \begin{cases} \mathbb{A}_1(\tau_s) - \mathbb{A}_2(\tau_s), & \text{if } \tau_s < \frac{\delta_2}{\theta_{ru_2}^2}, \\ 0, & \text{if } \tau_s \geq \frac{\delta_2}{\theta_{ru_2}^2}, \end{cases} \tag{31}$$

where

$$\mathbb{A}_1(\tau_s) = e^{-\left(\frac{m_{ru_2}\mathcal{T}_2}{\hat{\Omega}_{ru_2}\mathcal{T}_1}\right)} \sum_{c=0}^{m_{ru_2}-1} \frac{1}{c!}\left(\frac{m_{ru_2}\mathcal{T}_2}{\hat{\Omega}_{ru_2}\mathcal{T}_1}\right)^c \tag{32}$$

and

$$\begin{aligned} \mathbb{A}_2(\tau_s) = {} & \frac{1}{\Gamma(m_{ru_2})}\left(\frac{m_{ru_2}}{\hat{\Omega}_{ru_2}}\right)^{m_{ru_2}} e^{-\left(\frac{m_{ru_2}\mathcal{T}_2}{\hat{\Omega}_{ru_2}\mathcal{T}_1}\right)} \\ & \times \sum_{a=0}^{m_{u_2}-1}\sum_{b=0}^{a}\binom{a}{b}\frac{1}{a!}(\mathcal{T}_1)^b(-\mathcal{T}_2)^{a-b}\left(\frac{m_{u_2}}{k_2\Omega_{u_2}}\right)^a \\ & \times \sum_{d=0}^{b+m_{ru_2}-1}\frac{(b+m_{ru_2}-1)!}{d!}\left(\frac{\mathcal{T}_2}{\mathcal{T}_1}\right)^d \\ & \times \left(\frac{m_{ru_2}}{\hat{\Omega}_{ru_2}} + \frac{m_{u_2}\mathcal{T}_1}{k_2\Omega_{u_2}}\right)^{-(b+m_{ru_2}-d)}, \end{aligned} \tag{33}$$

with $\mathcal{T}_1 = \frac{\delta_2 - \theta_{ru_2}^2\tau_s}{\delta_1\,\tau_s}$ and $\mathcal{T}_2 = \frac{\phi_{ru_2}}{\delta_1\,\Delta_r}$.

Proof: See Appendix B. ∎

The involved CDFs in (30) can be readily deduced as

$$F_{\gamma_{su_2}^{\text{DT}}}(\tau_p) = \begin{cases} F_{|\hat{h}_{su_2}|^2}\left(\frac{\phi_{su_2}\tau_p}{\Delta_s(1-\theta_{su_2}^2\tau_p)}\right), & \text{if } \tau_p < \frac{1}{\theta_{su_2}^2}, \\ 1, & \text{if } \tau_p \geq \frac{1}{\theta_{su_2}^2}, \end{cases} \tag{34}$$

$$F_{\gamma_{ru_2,x_s}^{\text{DF}}}(\tau_p) = \begin{cases} F_{|\hat{h}_{ru_2}|^2}\left(\frac{\phi_{ru_2}\tau_p}{\Delta_r(\delta_1-\lambda_s\tau_p)}\right), & \text{if } \tau_p < \frac{\delta_1}{\lambda_s}, \\ 1, & \text{if } \tau_p \geq \frac{\delta_1}{\lambda_s}. \end{cases} \tag{35}$$

On substituting the results from (29) and (14) into (28), one can obtain the desired OP expression for the secondary network.

2) P-SIC: For this case, the OP of the secondary network can be computed through $\mathcal{P}_{u_{22}}$ with setting $k_2 = 0$ as

$$\mathcal{P}_{u_{22}} = \begin{cases} \mathbb{A}_3(\tau_s), & \text{if } \tau_s < \frac{\delta_2}{\theta_{ru_2}^2}, \\ 0, & \text{if } \tau_s \geq \frac{\delta_2}{\theta_{ru_2}^2}, \end{cases} \tag{36}$$

where

$$\begin{aligned} \mathbb{A}_3(\tau_s) = {} & \sum_{a=0}^{m_{ru_2}-1}\frac{1}{a!}\left(\frac{m_{ru_2}}{\hat{\Omega}_{ru_2}}\right)^a\left(\frac{\phi_{ru_2}\tau_s}{\Delta_r(\delta_2-\theta_{ru_2}^2\tau_s)}\right)^a \\ & \times e^{-\left(\frac{m_{ru_2}}{\hat{\Omega}_{ru_2}}\frac{\phi_{ru_2}\tau_s}{\Delta_r(\delta_2-\theta_{ru_2}^2\tau_s)}\right)}. \end{aligned} \tag{37}$$

Now, on inserting (36) into (29) and the result along with (14) into (28), one can fetch the requisite OP expression.

B. Asymptotic OP Analysis

The asymptotic OP for secondary network can be calculated as

$$\mathcal{P}_{\text{Sec}}^{\text{CSAT, asy}(\infty)}(r_{\text{th}}^s) = \big[1 - F_{\gamma_{sr}^{\text{DT}}}^{\text{asy}(\infty)}(\tau_p)\big]\big(1 - \mathcal{P}_{u_2}^{\text{asy}(\infty)}\big) + F_{\gamma_{sr}^{\text{DT}}}^{\text{asy}(\infty)}(\tau_p). \tag{38}$$

The expression for the joint probability term $\mathcal{P}_{u_2}^{\text{asy}(\infty)}$ is required for the computation of (38), which is derived in the succeeding subsections under I-SIC and P-SIC cases.

1) I-SIC: For the case of I-SIC, we derive the expression of $\mathcal{P}_{u_2}^{\text{asy}(\infty)}$ as

$$\mathcal{P}_{u_2}^{\text{asy}(\infty)} = \begin{cases} \mathcal{P}_{u_{21}}^{\text{asy}(\infty)} \times \mathcal{P}_{u_{22}}^{\text{asy}(\infty)}, & \text{if } \tau_p > \frac{\delta_1}{\lambda_s}, \\ \mathcal{P}_{u_{22}}^{\text{asy}(\infty)}, & \text{if } \tau_p \leq \frac{\delta_1}{\lambda_s}. \end{cases} \tag{39}$$

The probability term $\mathcal{P}_{u_{21}}^{\text{asy}(\infty)}$ in (39) can be calculated under Nakagami-*m* fading as

$$\begin{aligned} \mathcal{P}_{u_{21}}^{\text{asy}(\infty)} \approx {} & 1 - \sum_{i=0}^{H-1}\left\{ F_{\gamma_{su_2}^{\text{DT}}}^{\text{asy}(\infty)}\Big(\frac{i+1}{H}\,\tau_p\Big) - F_{\gamma_{su_2}^{\text{DT}}}^{\text{asy}(\infty)}\Big(\frac{i}{H}\,\tau_p\Big)\right\} \\ & \times F_{\gamma_{ru_2,x_s}^{\text{DF}}}^{\text{asy}(\infty)}\Big(\frac{H-i}{H}\,\tau_p\Big). \end{aligned} \tag{40}$$

The involved CDFs in (40) can be readily deduced similar to conditions like (34) and (35) as

$$F_{\gamma_{su_2}^{\text{DT}}}^{\text{asy}(\infty)}(\tau_p) = \frac{1}{\Gamma(m_{su_2})}\frac{1}{m_{su_2}}\left(\frac{m_{su_2}}{\hat{\Omega}_{su_2}}\right)^{m_{su_2}}\left(\frac{\tau_p\phi_{su_2}}{\Delta_s(1-\theta_{su_2}^2\tau_p)}\right)^{m_{su_2}} \tag{41}$$

and

$$F_{\gamma_{ru_2,x_s}^{\text{DF}}}^{\text{asy}(\infty)}(\tau_p) = \frac{1}{\Gamma(m_{ru_2})}\frac{1}{m_{ru_2}}\left(\frac{m_{ru_2}}{\hat{\Omega}_{ru_2}}\right)^{m_{ru_2}}\left(\frac{\tau_p\phi_{ru_2}}{\Delta_r(\delta_1-\lambda_s\tau_p)}\right)^{m_{ru_2}}, \tag{42}$$

and probability term $\mathcal{P}_{u_{22}}^{\text{asy}(\infty)}$ in (39) can be evaluated as

$$\begin{aligned} \mathcal{P}_{u_{22}}^{\text{asy}(\infty)} = {} & \sum_{a=0}^{m_{u_2}}\frac{1}{\Gamma(m_{u_2})}\frac{1}{m_{u_2}}\left(\frac{m_{u_2}}{\Omega_{u_2}}\right)^{m_{u_2}}\binom{m_{u_2}}{a} \\ & \times (T_1)^a\,(-T_2)^{(m_{u_2}-a)}\frac{1}{\Gamma(m_{ru_2})}\left(\frac{m_{ru_2}}{\hat{\Omega}_{ru_2}}\right)^{-a} \\ & \times \left[\Gamma(m_{ru_2}+a) - \frac{1}{(m_{ru_2}+a)}\left(\frac{m_{ru_2}T_2}{\hat{\Omega}_{ru_2}T_1}\right)^{(m_{ru_2}+a)}\right]. \end{aligned} \tag{43}$$

On substituting the results from (39) and (24) into (38), one can get the asymptotic OP expression for the secondary network. Thus, on computing the diversity order $d_{\text{Sec}}^{\text{I-SIC}} = -\lim_{\Delta\to\infty}\frac{\log(\mathcal{P}_{\text{Sec}}^{\text{CSAT, asy}(\infty)}(\Delta))}{\log(\Delta)}$, it implies that $d_{\text{Sec}}^{\text{I-SIC}} = 0$ for the I-SIC case.

2) P-SIC: In this case, the OP of the secondary network can be deduced through $\mathcal{P}_{u_{22}}^{\text{asy}(\infty)}$ under the setting $k_2 = 0$ as

$$\mathcal{P}_{u_{22}}^{\text{asy}(\infty)} = \begin{cases} \mathbb{A}_4(\tau_s), & \text{if } \tau_s < \frac{\delta_2}{\theta_{ru_2}^2}, \\ 0, & \text{if } \tau_s \geq \frac{\delta_2}{\theta_{ru_2}^2}, \end{cases} \tag{44}$$

where

$$\mathbb{A}_4(\tau_s) = \frac{1}{\Gamma(m_{ru_2})}\left[\Gamma(m_{ru_2}) - \frac{1}{m_{ru_2}}\left(\frac{m_{ru_2}}{\hat{\Omega}_{ru_2}}\right)^{m_{ru_2}}(\xi)^{m_{ru_2}}\right], \tag{45}$$

with $\xi = \frac{\tau_s\,\phi_{ru_2}}{\Delta_r(\delta_2-\theta_{ru_2}^2\tau_s)}$. Thus, on inserting (44) into (39) and the result along with (24) into (38), one can obtain the requisite OP expression. Hereby, we examine the diversity order $d_{\text{Sec}}^{\text{P-SIC}} = -\lim_{\Delta\to\infty}\frac{\log(\mathcal{P}_{\text{Sec}}^{\text{CSAT, asy}(\infty)}(\Delta))}{\log(\Delta)}$ to illustrate that $d_{\text{Sec}}^{\text{P-SIC}} = 0$. As a result, the corresponding OP curves would attain error floors in the high SNR region.

Algorithm 1: Optimal power allocation coefficient δ_1^*

Input: Initialize starting point $\delta_1 = 0.51$, step size $\varepsilon = 0.005$, stopping threshold $\mathbb{S}_{thre} = 0.0001$, initial value δ_1^*;

repeat
- $\mathcal{P}_{\text{Pri}}^{\text{CSAT}}$ is calculated using (23) with the provided δ_1;
- $\mathcal{P}_{\text{Sec}}^{\text{CSAT}}$ is calculated using (38) with the provided δ_1;
- **if** $\mathcal{P}_{Pri}^{CSAT} - \mathcal{P}_{Sec}^{CSAT} \geq \mathbb{S}_{thre}$ **then**
  - Assign: $\delta_1^* \leftarrow \delta_1$;
- **else**
  - break;
- **end**
- Assign: $\delta_1 \leftarrow \delta_1 + \varepsilon$;

until $\delta_1 < 1$;

Output: $\mathcal{P}_{\text{Pri}}^{\text{CSAT}*}(\delta_1^*)$ and $\mathcal{P}_{\text{Sec}}^{\text{CSAT}*}(\delta_2^*)$

C. Ceiling Effects in Secondary Network

Because of the limitations placed on the threshold τ_s, the SNC effect arises when node R is unable to transfer data to its destination U_2. This could be realized through (31) when $\tau_s \geq \frac{\delta_2}{\theta_{ru_2}^2}$ and from (14) when $\tau_p \geq \frac{1}{\theta_{sr}^2}$, or from (34) when $\tau_p \geq \frac{1}{\theta_{su_2}^2}$, the OP in (28) becomes unity, causing the secondary communication into outage. However, for an acceptable range of system parameters, especially power allocation parameter δ_2, $\frac{\delta_2}{\theta_{ru_2}^2}$ will be less than $\frac{1}{\theta_{sr}^2}$ or $\frac{1}{\theta_{su_2}^2}$, and hence the SNDR threshold for secondary communication is constrained by $\frac{\delta_2}{\theta_{ru_2}^2}$.

D. NOMA Power Optimization for Users' Fairness

Taking into account the projected FD-based CSAT scheme for OCR-NOMA system, each user's OP can be expressed as a function of the power allocation parameters provided by $\mathcal{P}_j^{\text{CSAT}}(\delta_1, \delta_2)$, where $j \in \{\text{Pri, Sec}\}$. We tackle the problem in such a way that each user's OP is minimized.

$$\mathbf{P}: \mathcal{P}_j^{\text{CSAT}\,*} = \min_{\delta_1, \delta_2} \mathcal{P}_j^{\text{CSAT}}(\delta_1, \delta_2), \tag{46}$$

$$\text{s.t. } (0 + \varrho) \leq \delta_k \leq (1 - \varrho), \quad \text{for } \varrho \approx 0, \tag{47}$$

$$\delta_1 + \delta_2 = 1, \tag{48}$$

where $k \in \{1, 2\}$. At high SNR, the derivatives of $\mathcal{P}_{\text{Pri}}^{\text{CSAT}}$ in relation to δ_1 derived from (23) and $\mathcal{P}_{\text{Sec}}^{\text{CSAT}}$ with respect to δ_1 derived from (38) are $\frac{\partial \mathcal{P}_{\text{Pri}}^{\text{CSAT}}}{\partial \delta_1}$ and $\frac{\partial \mathcal{P}_{\text{Sec}}^{\text{CSAT}}}{\partial \delta_1}$, respectively. As a result, $\mathcal{P}_{\text{Pri}}^{\text{CSAT}}$ and $\mathcal{P}_{\text{Sec}}^{\text{CSAT}}$ are found to be decreasing and increasing functions of δ_1, respectively. In this situation, solving $\mathcal{P}_{\text{Sec}}^{\text{CSAT}} = \mathcal{P}_{\text{Pri}}^{\text{CSAT}}$ will yield the optimal δ_1^* for attaining $\mathcal{P}_j^{\text{CSAT}\,*}$. The problem $\mathbf{P}$ can be simplified as follows:

$$\bar{\mathbf{P}}: \min_{\delta_1} (\mathcal{P}_{\text{Pri}}^{\text{CSAT}} - \mathcal{P}_{\text{Sec}}^{\text{CSAT}}), \tag{49}$$

$$\text{s.t. } \left(\frac{\tau_p(1 + \theta_{ru_1}^2)}{1 + \tau_p} + \varrho\right) \leq \delta_1 \leq (1 - \varrho). \tag{50}$$

It is hard to directly determine the exact closed-form solution for $\mathcal{P}_j^{\text{CSAT}\,*}$ because both $\mathcal{P}_{\text{Pri}}^{\text{CSAT}}$ and $\mathcal{P}_{\text{Sec}}^{\text{CSAT}}$ still retain the sum of many fraction terms at high SNR region. Therefore, in **Algorithm 1**, we offer a simple search strategy for finding the optimal δ_1^* with high accuracy $\mathbb{S}_{thre}$.

E. System Throughput

The system throughput refers to the average SE for the proposed FD OCR-NOMA system. It can be calculated as the sum of the target rates of primary and secondary networks that can be accomplished reliably as

$$\mathbb{S}_T^{\text{CSAT}} = \left[\left(1 - \mathcal{P}_{\text{Pri}}^{\text{CSAT}}(r_{\text{th}}^p)\right) r_{\text{th}}^p + \left(1 - \mathcal{P}_{\text{Sec}}^{\text{CSAT}}(r_{\text{th}}^s)\right) r_{\text{th}}^s\right]. \tag{51}$$

Letting $r_{\text{th}}^p = r_{\text{th}}^s = \mathfrak{R}$ in (51), we get $2\mathfrak{R}$ as the maximum achievable system throughput which could be achievable under ideal system conditions, when the OP goes to zero.

V. Ergodic Rate

The ergodic rate is a helpful indicator for evaluating performance when user rates are affected by the channel parameters. In a delay-tolerant transmission mode, the ergodic rate is defined as the opportunistic selection of target data transmission rates for users. By being constructed arbitrarily long, the codeword can span all the fading levels if needed. As a result, the ergodic rate calculation assumes that signals have been effectively decoded [38]. We describe and derive the analytical expressions for the ergodic rate for each of the users as well as the ESR for the overall system in this section. In addition, we investigate the ergodic rate at a high SNR, and thereby calculating the achievable slope analysis for the respective cases.

A. Ergodic Rate of U_1

Depending on the possibility that the signal x_s should be detected at R through a direct link, at U_1 by direct and relaying links, and at U_2 due to the SIC process [41], the ergodic rate at U_1 can be calculated as

$$R_{e,U_1} = E[\log_2(1 + \min\{\gamma_{sr}^{\text{DT}}, \gamma_{u_1}^{\text{MRC}}, \gamma_{u_2}^{\text{MRC}}\})]. \tag{52}$$

By defining $X \triangleq \min\{\gamma_{sr}^{\text{DT}}, \gamma_{u_1}^{\text{MRC}}, \gamma_{u_2}^{\text{MRC}}\}$, we can evaluate (52) as

$$\begin{aligned} R_{e,U_1} &= E[\log_2(1 + X)] \\ &= \int_0^\infty \log_2(1 + x)\, f_X(x)\, dx \\ &= \frac{1}{\ln 2} \int_0^\infty \frac{1 - F_X(x)}{1 + x}\, dx, \end{aligned} \tag{53}$$

where $F_X(x)$ is the CDF of X. We derive the expression of R_{e,U_1} in the following theorem.

Theorem 3: The ergodic rate R_{e,U_1} for FD-based CSAT scheme in OCR-NOMA system under Nakagami-*m* fading can be given by

$$R_{e,U_1} = \frac{1}{\ln 2} \frac{\pi}{N} \sum_{n=1}^{N} \left(\mathbb{B}_1 \times \mathbb{B}_2 \times \mathbb{B}_3\right) \frac{1}{1 - \Phi_n} \sqrt{1 + \Phi_n^2}, \tag{54}$$

with $\mathbb{B}_1$, $\mathbb{B}_2$ and $\mathbb{B}_3$ are given by

$$\mathbb{B}_1 = 1 - F_{\gamma_{sr}^{\text{DT}}}(x), \tag{55}$$

$$\begin{aligned} \mathbb{B}_2 = 1 - \sum_{i=0}^{H-1} &\left\{F_{\gamma_{su_1}^{\text{DT}}}\left(\frac{i+1}{H}\,\tau_p\right) - F_{\gamma_{su_1}^{\text{DT}}}\left(\frac{i}{H}\,\tau_p\right)\right\} \\ &\times F_{\gamma_{ru_1}^{\text{DF}}}\left(\frac{H - i}{H}\,\tau_p\right), \end{aligned} \tag{56}$$

$$\mathbb{B}_3 = 1 - \sum_{i=0}^{H-1} \left\{ F_{\gamma_{su_2}^{\text{DT}}}\Big(\frac{i+1}{H}\,\tau_p\Big) - F_{\gamma_{su_2}^{\text{DT}}}\Big(\frac{i}{H}\,\tau_p\Big) \right\} \times F_{\gamma_{ru_2,x_s}^{\text{DF}}}\Big(\frac{H-i}{H}\,\tau_p\Big), \tag{57}$$

where $\Phi_n = \cos\big(\frac{(2n-1)\pi}{2N}\big)$ and N is a parameter to ensure a complexity-accuracy trade-off.

Proof: See Appendix C. ∎

Finally, the requisite ergodic rate of U_1, i.e., R_{e,U_1}, can be calculated by putting the CDF expressions from (13), (14), (18), (34) and (35) into (55)-(57) and the results into (54).

B. Ergodic Rate of U_2

On the condition that the signal x_r from relaying link can be detected at node U_2 due to the SIC process [41], the ergodic rate at U_2 can be calculated as

$$R_{e,U_2} = E[\log_2(1+\gamma_{ru_2}^{\text{DF}})] = \frac{1}{\ln 2}\int_0^\infty \frac{1-F_{\gamma_{ru_2}^{\text{DF}}}(x)}{1+x}\,dx. \tag{58}$$

For the computation of (58), we further proceed with the derivation of the expressions for the ergodic rate at U_2 under I-SIC and P-SIC cases as $R_{e,U_2}^{\text{I-SIC}}$ and $R_{e,U_2}^{\text{P-SIC}}$, respectively, in the succeeding subsections.

1) I-SIC: By following the lemma presented below, the rate R_{e,U_2} in (58) can be assessed for the case of I-SIC.

Lemma 2: Under Nakagami-*m* fading, $R_{e,U_2}^{\text{I-SIC}}$ can be calculated using $F_{\gamma_{ru_2}^{\text{DF}}}(x)$ for FD-based CSAT scheme in OCR-NOMA system as

$$R_{e,U_2}^{\text{I-SIC}} = \frac{1}{\ln 2}\,\frac{\pi}{N}\sum_{n=1}^{N}\mathcal{P}_{u_{22}}\,\frac{1}{1-\Phi_n}\,\sqrt{1+\Phi_n^2}, \tag{59}$$

where $\mathcal{P}_{u_{22}}$ is derived in (31) for the I-SIC case.

Proof: By utilizing (31) and following the same methods outlined in Appendix C for (54), we get the result in (59). ∎

2) P-SIC: The $R_{e,U_2}^{\text{P-SIC}}$ can be accomplished in the condition of P-SIC using $F_{\gamma_{ru_2}^{\text{DF}}}(x)$, as shown in the following lemma.

Lemma 3: Under Nakagami-*m* fading, the $R_{e,U_2}^{\text{P-SIC}}$ for FD-based CSAT scheme in OCR-NOMA system can be calculated as

$$R_{e,U_2}^{\text{P-SIC}} = \frac{1}{\ln 2}\,\frac{\pi}{N}\sum_{n=1}^{N}\mathcal{P}_{u_{22}}\,\frac{1}{1-\Phi_n}\,\sqrt{1+\Phi_n^2}, \tag{60}$$

where $\mathcal{P}_{u_{22}}$ is presented in (36) for the P-SIC case.

Proof: We acquire the result (60) by using (36) and following the identical methods executed in Appendix C for (54). ∎

C. ESR Analysis

Now, we exploit the expressions from (54) and (59) to yield the analytical formula for the ESR of the OCR-NOMA system under I-SIC case as

$$R_{\text{ES}}^{\text{I-SIC}} = R_{e,U_1} + R_{e,U_2}^{\text{I-SIC}}. \tag{61}$$

While, summing up expressions (54) and (60) for the ESR under P-SIC case, we obtain

$$R_{\text{ES}}^{\text{P-SIC}} = R_{e,U_1} + R_{e,U_2}^{\text{P-SIC}}. \tag{62}$$

Owing to the non-ideal system imperfections such as LI, CEEs, HIs and the interference caused by the NOMA system, the ergodic rates R_{e,U_1}, $R_{e,U_2}^{\text{I-SIC}}$, and $R_{e,U_2}^{\text{P-SIC}}$ for FD-based CSAT scheme in OCR-NOMA system converge to ergodic rate ceilings in the high SNR region. Even, P-SIC can not solve the ergodic rate ceiling problem because it does not account for imperfect self-interference cancellation in a realistic way. This means that the residual LI always exists.

D. Asymptotic Ergodic Rate Analysis

The asymptotic behaviour of the ergodic rate is investigated in this section. It will provide more information about slope at high SNR region. We approximate the resulting ergodic rate expressions in (54), (59) and (60) for high SNR range ($\Delta_s, \Delta_r \to \infty$) to compute the possible slope analysis.

1) Asymptotic Ergodic Rate for U_1: Based on the ergodic rate expression in (53), on substituting (24), (26) and (40) into (83), (85) and (87), respectively, and the results into (82), we can obtain the $F_X(x)$. Then, after putting $F_X(x)$ into (53) and following the similar steps as used for (54) in Appendix C, we obtain the resultant asymptotic ergodic rate $R_{e,U_1}^{\text{asy}(\infty)}$ in (63).

2) Asymptotic Ergodic Rate for U_2 (I-SIC): Similarly, on substituting (43) into (59) and pursuing the analogous steps as used for (54) in Appendix C, we get the desired asymptotic ergodic rate $R_{e,U_2}^{\text{I-SIC, asy}(\infty)}$ in (64).

3) Asymptotic Ergodic Rate for U_2 (P-SIC): Likewise, on invoking (44) into (60) and carrying out the analogous steps as followed for (54) in Appendix C, we get the resultant asymptotic ergodic rate $R_{e,U_2}^{\text{P-SIC, asy}(\infty)}$ in (65).

E. Slope Analysis

In this subsection, we analyze the high SNR slope, which is a significant parameter in determining the ergodic rate in the high SNR region. The slopes of the derived ergodic rate expressions at a high SNR are obtained as follows:

$$S_{U_1} = \lim_{\Delta\to\infty}\frac{R_{e,U_1}^{\text{asy}(\infty)}(\Delta)}{\log(\Delta)}, \tag{66}$$

$$S_{U_2}^{\text{I-SIC}} = \lim_{\Delta\to\infty}\frac{R_{e,U_2}^{\text{I-SIC, asy}(\infty)}(\Delta)}{\log(\Delta)}, \tag{67}$$

$$S_{U_2}^{\text{P-SIC}} = \lim_{\Delta\to\infty}\frac{R_{e,U_2}^{\text{P-SIC, asy}(\infty)}(\Delta)}{\log(\Delta)}. \tag{68}$$

Now, on substituting (63), (64) and (65) into (66), (67) and (68), respectively, and doing some calculation, we can achieve the corresponding high SNR slopes as $S_{U_1} = 0$, $S_{U_2}^{\text{I-SIC}} = 0$ and $S_{U_2}^{\text{P-SIC}} = 0$. It is due to the system's inherent imperfections, such as LI, CEEs, and HIs, that are unavoidable. As a result, the corresponding ergodic rate curves converge to the ergodic rate ceiling in the high SNR region.

VI. Deep Neural Network Framework Design

This section introduces the DNN framework for predicting the ergodic rate and ESR with minimal computational complexity and short run time. This is in contrast to the fact that analytical evaluation and Monte Carlo simulations are difficult and time-consuming.

$$R_{e,U_1}^{\text{asy}(\infty)} = \frac{1}{\ln 2}\frac{\pi}{N}\sum_{n=1}^{N}\Bigg[1-\sum_{a=0}^{m_{sr}}\frac{1}{\Gamma(m_{sr})}\frac{1}{m_{sr}}\left(\frac{m_{sr}}{\hat{\Omega}_{sr}}\right)^{m_{sr}}\left(\frac{\tau_p}{\Delta_s\vartheta}\right)^{m_{sr}}\binom{m_{sr}}{a}\left(\Delta_r(1+\theta_{rr}^2)\right)^a\left(\phi_{sr}\right)^{(m_{sr}-a)}\frac{1}{\Gamma(m_{rr})}\left(\frac{m_{rr}}{\Omega_{rr}}\right)^{m_{rr}}$$
$$\times\,(m_{rr}-1+a)!\left(\frac{m_{rr}}{\Omega_{rr}}\right)^{-(m_{rr}+a)}\Bigg]\Bigg[1-\sum_{i=0}^{H-1}\left\{F_{\gamma_{su_1}^{\text{DT}}}^{\text{asy}(\infty)}\left(\frac{i+1}{H}\,\tau_p\right)-F_{\gamma_{su_1}^{\text{DT}}}^{\text{asy}(\infty)}\left(\frac{i}{H}\,\tau_p\right)\right\}F_{\gamma_{ru_1}^{\text{DF}}}^{\text{asy}(\infty)}\left(\frac{H-i}{H}\,\tau_p\right)\Bigg]$$
$$\times\Bigg[1-\sum_{i=0}^{H-1}\left\{F_{\gamma_{su_2}^{\text{DT}}}^{\text{asy}(\infty)}\left(\frac{i+1}{H}\,\tau_p\right)-F_{\gamma_{su_2}^{\text{DT}}}^{\text{asy}(\infty)}\left(\frac{i}{H}\,\tau_p\right)\right\}F_{\gamma_{ru_2,x_s}^{\text{DF}}}^{\text{asy}(\infty)}\left(\frac{H-i}{H}\,\tau_p\right)\Bigg]\frac{1}{1-\Phi_n}\sqrt{1+\Phi_n^2}. \tag{63}$$

$$R_{e,U_2}^{\text{I-SIC, asy}(\infty)} = \frac{1}{\ln 2}\frac{\pi}{N}\sum_{n=1}^{N}\Bigg[\sum_{a=0}^{m_{u_2}}\frac{1}{\Gamma(m_{u_2})}\frac{1}{m_{u_2}}\left(\frac{m_{u_2}}{\Omega_{u_2}}\right)^{m_{u_2}}\binom{m_{u_2}}{a}\left(T_1\right)^a\left(-T_2\right)^{(m_{u_2}-a)}\frac{1}{\Gamma(m_{ru_2})}\left(\frac{m_{ru_2}}{\hat{\Omega}_{ru_2}}\right)^{-a}$$
$$\times\Bigg[\Gamma(m_{ru_2}+a)-\frac{1}{(m_{ru_2}+a)}\left(\frac{m_{ru_2}T_2}{\hat{\Omega}_{ru_2}T_1}\right)^{(m_{ru_2}+a)}\Bigg]\Bigg]\frac{1}{1-\Phi_n}\sqrt{1+\Phi_n^2}. \tag{64}$$

$$R_{e,U_2}^{\text{P-SIC, asy}(\infty)} = \frac{1}{\ln 2}\frac{\pi}{N}\sum_{n=1}^{N}\Bigg[\frac{1}{\Gamma(m_{ru_2})}\Bigg[\Gamma(m_{ru_2})-\frac{1}{m_{ru_2}}\left(\frac{m_{ru_2}}{\hat{\Omega}_{ru_2}}\right)^{m_{ru_2}}\left(\frac{\tau_s\,\phi_{ru_2}}{\Delta_r(\delta_2-\theta_{ru_2}^2\tau_s)}\right)^{m_{ru_2}}\Bigg]\Bigg]\frac{1}{1-\Phi_n}\sqrt{1+\Phi_n^2}. \tag{65}$$

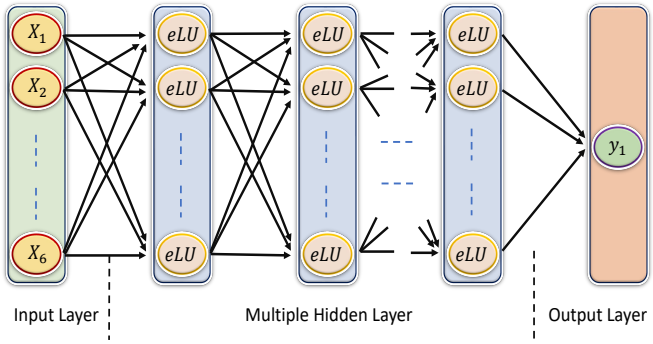

Fig. 2: DNN deployment architecture.

TABLE I: DNN training and testing input parameters.

Parameters (Input)	Values	Parameters (Input)	Values
SNR ($\Delta_s = \Delta_r$)	$[0, 40]$	Rate ($r_{\text{th}}^p = r_{\text{th}}^s$)	$[0.1, 1]$
Level of HIs (θ_0)	$[0, 0.4]$	Power factor (δ_1)	$[0.51, 0.99]$
CEEs' Variance (ϵ^2)	$[0, 1]$	Residual IS (k_2)	$[0, 0.5]$

A. Dataset Generation Approach

The dataset for this research was created using the functions given in (54), (59), and (60) because these functions are related to system factors like SNR ($\Delta_s = \Delta_r$), level of HIs (θ_0), CEEs' variance (ϵ^2), rate ($r_{\text{th}}^p = r_{\text{th}}^s$), power factor ($\delta_1$), and residual IS ($k_2$). All system parameters are used as training sample input variables and are generated in a consistent manner based on the network size. The resulting dataset $\mathcal{K}$ has a row vector containing dataset$[k] = [\mathcal{X}[k], \mathcal{Y}^{\text{sim}}]$ for each sample k, where $\mathcal{X}[k]$ is a feature vector comprising all of the input variables specified in Table I. Every feature vector $\mathcal{X}[k]$ is utilized to build actual ergodic rate and ESR sets from (54), (59), (60), (61), and (62), and each one is fed into simulation and given a unique output $\mathcal{Y}^{\text{sim}}$. Additionally, we discover that $\mathcal{X}[k]$ and $\mathcal{Y}^{\text{sim}}$ must be normalized before being provided to the DNN, where $\mathcal{X}^{\text{norm}}[k] = (\mathcal{X}[k] - \mathcal{X}^{\min}[k])/(\mathcal{X}^{\max}[k] - \mathcal{X}^{\min}[k])$ and $\mathcal{Y}^{\text{norm}} = (\mathcal{Y}^{\text{sim}} - \mathcal{Y}^{\min})/(\mathcal{Y}^{\max} - \mathcal{Y}^{\min})$ aim to improve learning (i.e., rapid convergence), achieve better projected results, and avoid the over-fitting issue. There are benefits to normalizing and encoding data first, then separating it. The training and test data both contain more information when all the source data is normalized and encoded first, followed by splitting the data, as opposed to splitting the data first. Practically, normalizing and encoding the source data first, and then splitting, is more simpler than splitting first and then normalizing-encoding on two datasets. Furthermore, if we normalize and encode our data first, we will not encounter a scenario in which we can not encode a categorical test predictor because it did not present in the training data. We use linear functions for output units and nonlinear activation functions for hidden-level units. In this situation, we can normalize the target output from the target's perspective. The resulting dataset has a total of 10×10^5 samples, with 80% of them being used for training ($\mathcal{K}_{trn}$), and the rest being split evenly between validation ($\mathcal{K}_{val}$) and testing ($\mathcal{K}_{tes}$). In most circumstances, we have found that this number of samples is adequate to get highly correct estimates.

B. DNN Learning Model

As shown in Fig. 2, a typical DNN is a feed-forward neural network with one input layer, many hidden layers, and one output layer. The input layer has 6 neurons, each of which corresponds to one of the 6 parameters listed in Table I. We utilize an exponential linear unit (eLU) activation function to perform a threshold operation for each input parameter x at each hidden layer. Any number less than zero is scaled up to zero, and the following is an example of how eLU works:

$$eLU(x) = \begin{cases} \alpha\,(e^x - 1), & \text{if } x < 0, \\ x, & \text{if } x \geq 0, \end{cases} \tag{69}$$

where α is a constant value set to 1. Due to its near-linear nature, the eLU activation function offers considerable advantages over the rectified exponential linear unit (ReLU), scaled exponential linear unit (SeLU), hyperbolic tangent (Tanh), Softmax, and Softplus activation functions. More specifically, it facilitates easier optimization and computational simplicity, and it overcomes the issue of vanishing gradients. In the meantime, when the input data are extremely high or low, the Tanh methods run into the problem of vanishing gradients, resulting in increasing computing complexity [42]. When the inputs approach zero/negative [42], the fading ReLU problem becomes obvious. Since the regression problem intends to estimate an output value without any further conversions, the output layer, which only contains one neuron, applies the linear activation function to produce the anticipated ergodic rate/ESR value, $\mathcal{Y}^{\text{sim}}$ [23]. We take an utterly connected layer, in which the activation $\mathcal{A}_n^m$ of the n-th neuron in the m-th layer is connected to activations in the $(m-1)$-th layer as follows:

$$\mathcal{A}_n^m = eLU\bigg(\sum_{i=1}^{\mathcal{Q}_{m-1}} \mathcal{W}_{n,i}^m \mathcal{A}_i^{m-1} + \mathcal{C}_n^m\bigg), \tag{70}$$

where $\mathcal{Q}_{m-1}$ is the number of neurons in the $(m-1)$-th layer. In the $(m-1)$-th layer, $\mathcal{W}_{n,i}^m$ stands for the weight that connects to the (i)-th neuron, and finally, at the (m)-th layer, $\mathcal{C}_n^m$ denotes a scalar bias.

C. Ergodic Rate and ESR Real-Time Prediction

The DL framework comprises two phases: training and prediction. The neural network learns input-output relationships offline during the training phase by employing the adaptive moment estimation (Adam) optimization technique, which aims to optimise model parameters based on the dataset. During the backpropagation operation, Adam is used to calculate/update the weights and biases for the considered DNN model, when compared to other learning optimization methods (such as momentum, stochastic gradient descent, RMSProp, and nesterov accelerated gradient) [43]. Adam shows greater performance benefits in the form of training speed. Let $\mathcal{Y}^k$ and $\bar{\mathcal{Y}}^k$ represent the DNN model's actual and expected output values for the (k)-th testing datasets. The mean-square error (MSE) between estimated and forecasted values can be determined using the following loss function:

$$\text{Loss}\big(\mathcal{Y}^k, \bar{\mathcal{Y}}^k\big) = \frac{1}{\mathcal{K}_{tes}} \sum_{k=1}^{\mathcal{K}_{tes}} \big(\mathcal{Y}^k - \bar{\mathcal{Y}}^k\big)^2. \tag{71}$$

RMSE is determined as follows:

$$\text{RMSE} = \sqrt{\frac{1}{\mathcal{K}_{tes}} \sum_{k=1}^{\mathcal{K}_{tes}} \big(\mathcal{Y}^k - \bar{\mathcal{Y}}^k\big)^2}, \tag{72}$$

where $\mathcal{K}_{tes}$ denotes the total number of datasets in the test-set.

The resultant DNN model, which includes weights and biases, can be represented in a compact mapping function as $\mathcal{F}(.)$, when the offline training is finished. When a DNN is properly trained, it can make highly accurate, real-time predictions. When new data is available at the input, we apply the DNN model to estimate the ergodic rate and ESR values. The input data was organized as an $\mathcal{X}$-vector, which is arranged as $\mathcal{X} = [\Delta_s = \Delta_r, \theta_0, \epsilon^2, r_{\text{th}}^p = r_{\text{th}}^s, \delta_1, k_2]$. The predicted process can be summed up as follows:

$$\bar{\mathcal{Y}} = \mathcal{F}(\mathcal{X}). \tag{73}$$

Consequently, $\mathcal{O}_j = [\mathcal{X}_j, \mathcal{Z}_j^1, ..., \mathcal{Z}_j^t, ...\mathcal{Z}_j^T]$ can be used to represent the j-th training samples, with a total number of targeted outputs being the T, where $\mathcal{Z}_j^t$, $t \in \{1, ..., T\}$, stands for the target outputs, such as R_{e,U_1}, $R_{e,U_2}^{\text{I-SIC}}$, $R_{e,U_2}^{\text{P-SIC}}$, $R_{\text{ES}}^{\text{I-SIC}}$, $R_{\text{ES}}^{\text{P-SIC}}$ for the j-th sample and $\mathcal{O} = \{\mathcal{O}_1, \mathcal{O}_2, ...\}$ for the training set. The ergodic rate and ESR may be estimated in a short time by the generated DNN model using a low-latency inference approach in (73). DNN settings can be adaptively configured to obtain the lowest error during the training phase since the capacity of DNN can be upgraded by adding additional hidden layers or neurons/hidden units network.

D. DNN Complexity Analysis

The number of floating-point operations (FLOPs) per second, which is depending on the number of weights and biases of the network, is used to measure the computational complexity of the proposed DNN model. Let the number of input variables (i.e., $v_{in} = 6$), the number of input layer neurons (i.e., $v_0 = 150$), the number of m-th hidden layer neurons (i.e., $v_{hid}[m] = 150$) with $m \in \{1, 2, ..., 4\}$, and the number of output layer neuron (i.e., $v_{out} = 1$). The DNN has the following number of parameters:

$$\begin{aligned}\mathcal{N}_{Param} = {} & v_{in} \times v_0 + v_0 + v_0 \times v_{hid}[1] + v_{hid}[1] \\ & + ... + v_{hid}[m] \times v_{hid}[m+1] + v_{hid}[m+1] \\ & + ... + v_{hid}[4] \times v_{out} + v_{out}.\end{aligned} \tag{74}$$

The DNN has the following number of FLOPs:

$$\begin{aligned}\mathcal{N}_{FLOPs} = {} & v_{in} \times v_0 \times 2 + v_0 + v_0 \times v_{hid}[1] \times 2 + v_{hid}[1] \\ & + ... + v_{hid}[m] \times v_{hid}[m+1] \times 2 + v_{hid}[m+1] \\ & + ... + v_{hid}[4] \times v_{out} \times 2 + v_{out}.\end{aligned} \tag{75}$$

As a consequence, the calculated DNN model comprises about 91k (91,801) parameters and 182k (182,851) FLOPs.

VII. Numerical and Simulation Results

We pursue numerical investigation for the suggested FD CSAT scheme in this section, as well as Monte-Carlo simulations in MATLAB version R2022a to validate our theoretical conclusions. The figures in this section show a tight relationship between simulation and numerical results, confirming the correctness of our findings in Sections III-VI. Unless otherwise provided, we set the system parameters shown in Table II. We also set $\Delta_s = \Delta_r$ as the SNR, $\theta_{ts} = \theta_{tr} = \theta_{rsu_1} = \theta_{rsu_2} = \theta_{rsr} = \theta_{rrr} = \theta_{rru_1} = \theta_{rru_2} = \theta_0$ as the level of HIs such that $\theta_{su_1} = \theta_{su_2} = \theta_{sr} = \theta_{rr} = \theta_{ru_1} = \theta_{ru_2} = \sqrt{2}\theta_0$. The EVMs [36] are used to determine these parameters.

TensorFlow 2.8.0 is used to create a DNN model with 4 hidden layers and 150 hidden neurons per layer in Python 3.7.13 associated with Keras 2.8.0. The DNN is trained from start to finish in 70 epochs, with the weights randomly initialised using the Adam optimizer and a gradient decay value of 0.95. The learning rate is initially set to 10^{-3} (after 20

Algorithm 2: DNN Training and Testing Procedure

Input: Set up the DNN model with $\mathcal{X} = [\Delta_s = \Delta_r, \theta_0, \epsilon^2, r_{\text{th}}^p = r_{\text{th}}^s, \delta_1, k_2]$ as the input variables;

Parameters: Set up the important parameters for the hidden and output layers, including the neuron per layer, activation, kernel, learning rate, epochs, etc;

Output: Specify $\mathcal{Z}_j^t$ as the target output from the vector $\mathcal{O}_j = [\mathcal{X}_j, \mathcal{Z}_j^1, ..., \mathcal{Z}_j^t, ...\mathcal{Z}_j^T]$;

while *The number of epochs is lower than the number specified in the setting* **do**

  Perform forward DNN procedure to obtain the output layer data result, which is denoted as $\mathcal{Z}_{out}^t$;

  Compute the loss function $\text{Loss}(\mathcal{Y}^k, \bar{\mathcal{Y}}^k) = \frac{1}{\mathcal{K}_{tes}} \sum_{k=1}^{\mathcal{K}_{tes}} \left(\mathcal{Y}^k - \bar{\mathcal{Y}}^k\right)^2$, which is the MSE over testing dataset;

  To find the best solution, use Adam optimization method to compute the correction parameter and update the parameters with the algorithm;

end

Display the training and validation curves after testing the trained DL with the test data;

Save the trained output in a file named "_.h5" that includes the input parameters;

epochs fall 90%). The inherent complexity (or perplexity) of our dateset will determine the appropriate number of epochs. Start with a value that is three times the number of columns in our data as a general rule of thumb. We try again with a larger number if we discover that the model is still improving after all epochs have finished. We try again with a lower value if we discover that the model stopped improving long before the final epoch because we might be over-training. We may need to dramatically increase the number of epochs to help the neural network learn the structure of the data if there are few records in our dataset or if many records are failing validation. On our training dataset, it is crucial to select a good value for our model's learning rate, one that finds the lowest loss with the fewest iterations and converges quickly. One strategy for solving this issue is to experiment with various learning rate values and pick the one that yields the lowest loss without taking an excessive amount of time to converge. All of the tests were performed on a computer with specification i7-7700 (CPU), 16 GB (RAM), and GeForce GTX 1080 8 GB (GPU). **Algorithm 2** illustrates the detailed training and testing procedure for the DNN approach.

Fig. 3 plots the OP versus SNR curves for the primary network using different values of r_{th}^p under both perfect (ideal) hardware ($\theta_0 = 0$) and the imperfect hardware ($\theta_0 = 0.2$). While satisfying the CSAT requirement as given in Section III-D, we choose acceptable values of δ_1. The OP curves are also drawn for the PDLT, HD-based CSAT, and OMA-based CSAT schemes, which are used for comparison purposes. To begin, one can verify that the analytical and simulated curves are well wedged over the whole SNR region. The

TABLE II: Simulation Parameters [with $i \in \{1, 2\}$].

Parameters	Values
Average fading powers ($\hat{\Omega}_{su_i}$, $\hat{\Omega}_{sr}$, $\hat{\Omega}_{ru_i}$) [30]	0.1, 0.1, 1, 0.7, 1
Fading severity parameters (m_{su_i}, m_{sr}, m_{rr}, m_{ru_i}, m_{u_2}) [29]	1, 1, 2, 2, 2, 2, 2
Average power gains of LI and IS channel (Ω_{rr}, Ω_{u_2}) [33]	0.1, 1
Level of HIs [36], [37] ($\theta_{su_i} = \theta_{sr} = \theta_{ru_i} = \theta_{rr} = \sqrt{\bar{\theta}}\theta_0$)	$\theta_0 = 0$, 0.1, 0.2, 0.3
Variance of the CEEs [29] ($\epsilon_{su_i}^2 = \epsilon_{sr}^2 = \epsilon_{ru_i}^2 = \epsilon^2$)	$\epsilon^2 = 0.005$
Block duration (T) [27]	1 sec
Target rate ($r_{\text{th}}^p = r_{\text{th}}^s$) [27]	0.5 bps/Hz
Noise variance (σ^2) [27]	1
Level of stairways conjecture (H) [40]	50
Complexity-accuracy trade-off parameter (N)	100

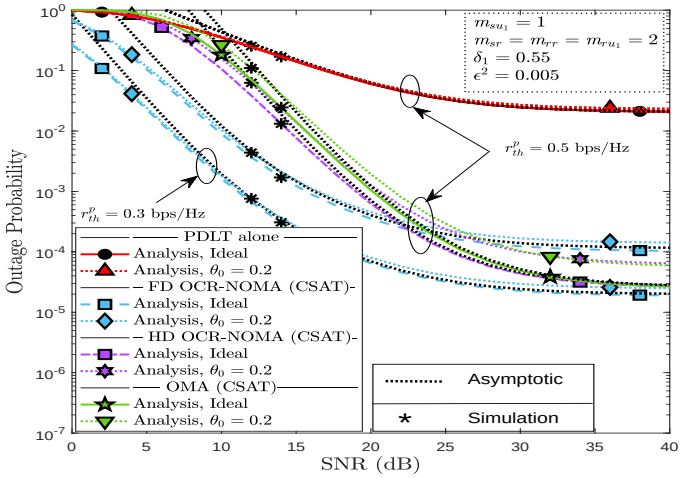

Fig. 3: OP performance of the primary network.

asymptotic curves are likewise well aligned with the analytical and simulated curves in the high SNR regime. In addition, the FD CSAT scheme has a significantly smaller OP than the PDLT scheme for the fixed target rate. In the lower SNR region, the FD CSAT scheme outperforms HD CSAT and OMA CSAT schemes. However, in the higher SNR region, HD CSAT and OMA CSAT schemes outperform FD CSAT. This is due to the fact that, in the case of FD CSAT, the impact of LI becomes dominating at high SNR, and thereby degrades its outage performance. On the contrary, in the low SNR regime, the multiplexing gain of FD CSAT predominates over the HD CSAT and OMA CSAT scheme. Although the incorporation of HIs ($\theta_0 = 0.2$) degrades the performance of the primary network, its impact is more noticeable at higher target rates. Moreover, the HIs have a greater influence on the HD scheme at the high SNR regime. Although the LI affects the cooperative FD relay diversity performance, the proposed FD OCR-NOMA with CSAT scheme attains performance advantage by exploiting the DT-link.

Fig. 4 depicts the OP performance of secondary network under both P-SIC and I-SIC cases. For this, we fix the target rate at $r_{\text{th}}^p = r_{\text{th}}^s = 0.5$ bps/Hz and HIs at $\theta_0 = 0, 0.2$. To begin, one can verify that the analytical and simulated curves are well aligned across the whole SNR region. The asymptotic curves are likewise well aligned with the analytical and simulated

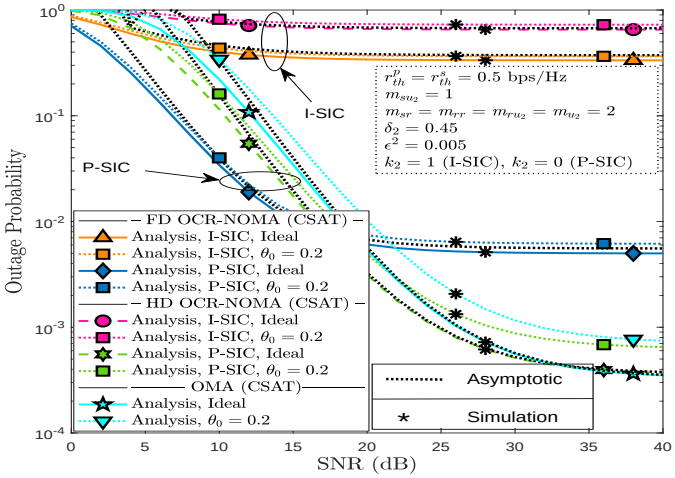

Fig. 4: OP performance of the secondary network.

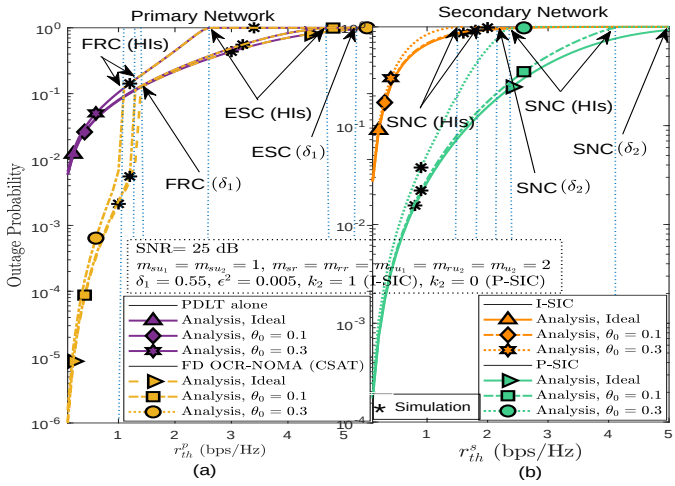

Fig. 5: Ceiling effects of the primary and secondary networks.

curves in the high SNR regime. The OP in the I-SIC case is much higher than the P-SIC case under FD/HD-based CSAT schemes. For the P-SIC case, FD CSAT outperforms the HD CSAT and OMA CSAT in the low SNR regime, while HD CSAT and OMA CSAT outperform FD CSAT in the high SNR region. Whereas, for the I-SIC case, FD CSAT can always perform better than HD CSAT. Further, in comparison to FD CSAT, the performance loss due to HIs is more apparent for HD CSAT and OMA CSAT.

Fig. 5(a) shows the OP performance versus target rate r_{th}^p plot of the primary network for FD CSAT scheme. In this figure, we show how the primary network can handle a maximum data rate and a tolerance limit on the HIs level until an outage owing to ceiling effects occurs. We set the SNR to 25 dB and the θ_0 values to 0, 0.1, and 0.3 to draw the various curves. Correspondingly, we choose δ_1 based on whether or not it meets the QoS criterion outlined in Section III-D. To begin with, we can see that when the target rate rises, the performance of the primary network degrades. Furthermore, the OP curves associated with HIs depart from the ideal behavior as the r_{th}^p increases. When the threshold for CSAT scheme surpasses $\tau_p = \frac{\delta_1}{\lambda_p}$ [refer to (18)], the FRC phenomenon, indicated as FRC (HIs), emerges, rendering relay cooperation ineffectual, and the primary network's OP performance reverting to the

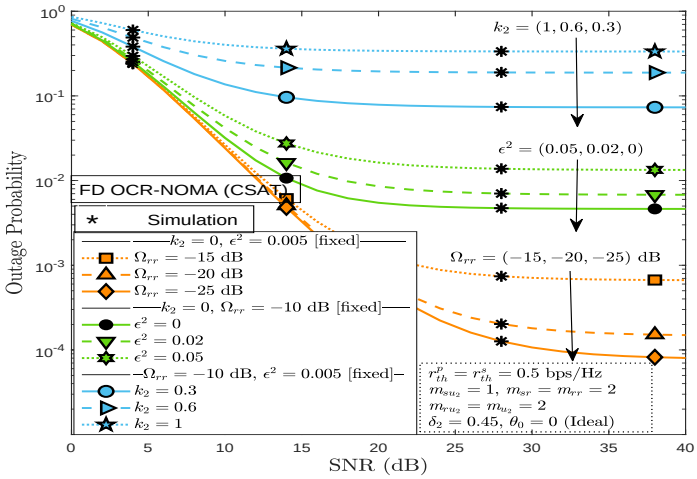

Fig. 6: Impact of LI, CEEs, and I-SIC on secondary network.

PDLT scheme. When the FRC effect is examined for ideal curves, it is revealed that it occurs at significantly higher target rate values. This is due to the condition $\delta_1 < 1$ being violated, which is indicated in the figure as FRC (δ_1). Hereafter, the primary OP approaches unity when r_{th}^p goes further to reach the ESC threshold $\tau_p = \frac{1}{\theta_{su_1}^2}$ [refer to (13)]. Furthermore, the relative accretion of τ_p in the FRC threshold for the curves resulting from the CSAT technique can be seen. Fig. 5(b) shows the secondary network's OP performance in comparison to the target rate r_{th}^s. We set SNR to 25 dB and θ_0 to 0, 0.1, and 0.3 for plotting the different curves. We set the value of δ_2 in the same way that we did with $r_{\text{th}}^s = r_{\text{th}}^p$ before. When r_{th}^s rises, as expected, the curves with HIs deviate from the ideal one. The SNC effect therefore happens for the P-SIC case at $\tau_s \geq \frac{\delta_2}{\theta_{ru_2}^2}$ [refer to (36)]. On the other hand, because of the additional impact of IS channel power increase, the SNC effect occurs comparatively at lower values of target rate r_{th}^s in the I-SIC mode.

To further examine the relative impacts of LI, CEEs, and I-SIC on the OP performance of secondary network, we plot Fig. 6 by varying the values of Ω_{rr}, ϵ^2 and k_2. For a fixed level of I-SIC ($k_2 = 0$) and CEEs ($\epsilon^2 = 0.005$), the OP performance of secondary network improves with the decreasing values of $\Omega_{rr} = -15, -20, -25$ dB. Now, on fixing the I-SIC ($k_2 = 0$) and LI ($\Omega_{rr} = -10$ dB), the OP performance improves significantly with the decrease in the level of CEEs ($\epsilon^2 = 0.05, 0.02, 0$). At last, with the fixed LI ($\Omega_{rr} = -10$ dB) and CEEs ($\epsilon^2 = 0.005$), one can see that the OP performance improves significantly with the decrease in the level of I-SIC ($k_2 = 1, 0.6, 0.3$).

Fig. 7 shows the effect of the power allocation coefficients δ_1 and δ_2 on a user's OP at various SNR levels. Regardless of how their SNR varies, as δ_1 increases, the OP of the primary network decreases while the OP of the secondary network increases. As we can see from the plot, there is a minor change in OPs at high SNR values. Furthermore, there is a performance trade-off between primary and secondary networks. We have presented **Algorithm 1** to identify the optimal value of δ_1 in order to establish a reasonable balance between OPs of primary and secondary networks.

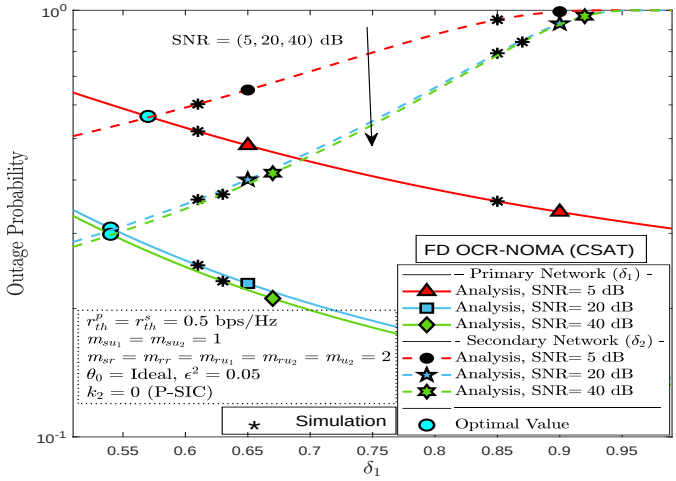

Fig. 7: Impact of power allocation coefficients.

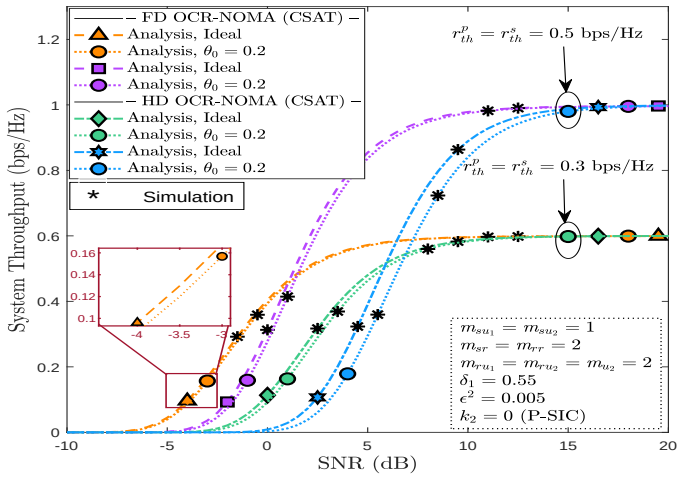

Fig. 8: System throughput versus SNR plots.

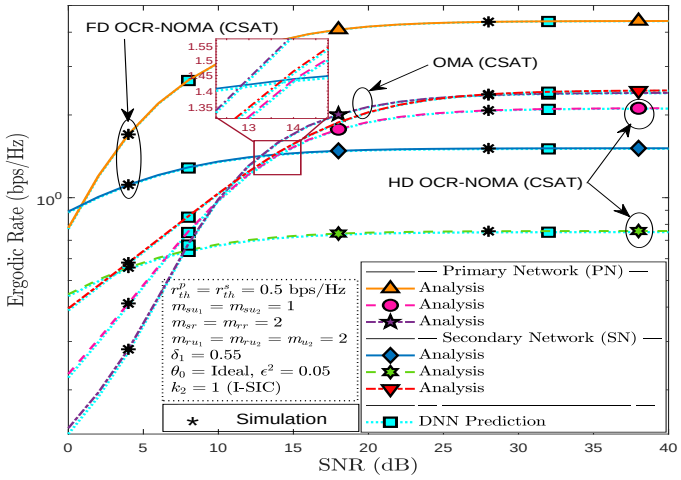

Fig. 9: Ergodic rate versus SNR plots.

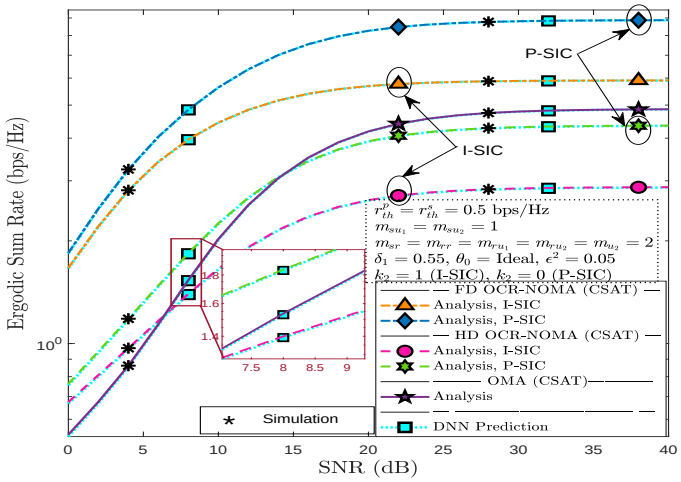

Fig. 10: ESR versus SNR plots.

Fig. 8 plots the system throughput curves for the FD/HD-based CSAT schemes. We can see that, in the low SNR region, the system throughput falls as the target rate increases. Alternatively, the system throughput rises until it reaches a particular level of SNR, at which it becomes saturated. This saturation in throughput occurs at a reasonably high SNR for a larger value of target rate. We can clearly see that the FD CSAT has a higher throughput than HD CSAT for a fixed value of SNR. Furthermore, in contrast to FD CSAT scheme, the throughput degradation due to HIs is more prominent for the HD CSAT scheme.

Fig. 9 shows the ergodic rate comparison of primary network and secondary network in anticipation of transmit SNR. We set the target rate at $r_{\text{th}}^p = r_{\text{th}}^s = 0.5$ bps/Hz and CEEs (ϵ^2) to 0.05 for plotting the different curves. It should be noticed that in a low transmit SNR region, the ergodic rates of primary network and secondary network increase rapidly. However, in a high transmit SNR region, the ergodic rate curves become constant. It can also be seen from the graph that primary network has a substantially higher capacity than secondary network in mid-to-high SNR region. This is because, in primary transmission, x_s can be detected at nodes R, U_1 and U_2, but in secondary transmission, x_r can be detected at U_2 node only. In the FD system, users attain a higher ergodic rate than in the similar HD and OMA systems in low SNR region, where additional time periods are required to complete the transmission of symbols. Interestingly, the simulation curves, as can be seen, completely follow the analytical formulas stated in (54), (59), and (60) and also the DNN prediction.

Fig. 10 compares the ESR of our proposed FD/HD/OMA based CSAT schemes OCR-NOMA system under both P-SIC and I-SIC cases. For this, we fix the target rate at $r_{\text{th}}^p = r_{\text{th}}^s = 0.5$ bps/Hz and HIs at $\theta_0 = 0$. It is obvious from the graph that, under P-SIC, FD/HD CSAT schemes have a significantly higher capacity gain at high SNR as compared to the I-SIC case. This is because, under I-SIC, the level of residual IS coefficient (k_2) has a substantial impact on the capacity gain, especially at high SNR. In the FD system, users attain a higher ESR than in the similar HD and OMA systems, where additional time periods are required to complete the transmission of symbols. The DNN prediction outcomes are almost identical to the analytical and simulation results, demonstrating DNN's superior prediction capacity.

The RMSE is evaluated as a function of number of hidden neurons in Fig. 11(a) to provide some insights into the chosen DNN model. It has been noted that the ESR is projected to have a lower RMSE when the DNN model includes more hidden

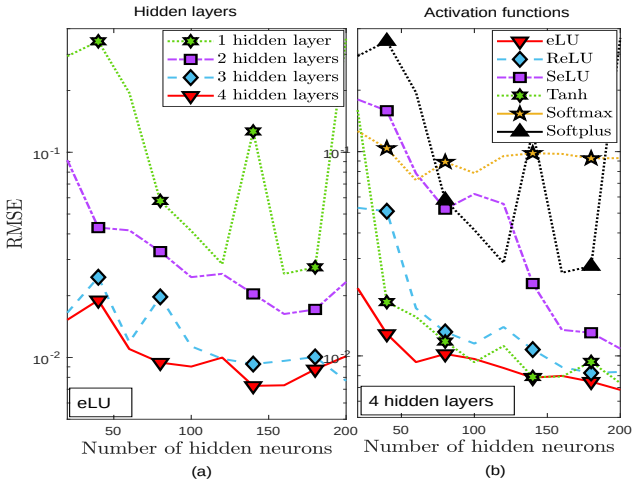

Fig. 11: RMSE versus number of hidden neurons. (a) Hidden layers. (b) Activation functions.

layers[4]. The predicted DNN model with several hidden layers can generalise datasets, resulting in increased network capacity, while a single layer DNN is unable to learn complicated patterns in some high dimensional dataset, resulting in a large RMSE and small network capacity. Fig. 11(b) shows the RMSE comparison of eLU with other common activation functions such as ReLU, SeLU, Tanh, Softmax, and Softplus. As one can see, when the number of hidden neurons rises, Softmax becomes the poorest activation function, while eLU becomes the best. Furthermore, Tanh and SeLU are two activation functions that perform similar to eLU in terms of RMSE and quick convergence. Finally, the proposed system's DNN assessment, analytical evaluation, and Monte Carlo simulation are compared in terms of execution time. The results demonstrate that obtaining ESR values using DNN prediction only takes 0.0216 seconds. In the meantime, the Monte Carlo simulation takes 8.3854 seconds to get the ESR values, and the analytical evaluation takes 0.0492 seconds. The analytical evaluation and DNN prediction values are used to calculate the RMSE, which is 0.0087.

VIII. Conclusion

We assessed the performance of OCR-NOMA system using FD CSAT scheme under the presence of HIs, CEEs, LI, and I-SIC. We derived the closed-form OP expressions for the primary and secondary networks in Nakagami-*m* fading environment and results were compared to the benchmark PDLT and HD/OMA CSAT schemes. We also computed system throughput and ESR to gain further insights. In addition, we provided a guidance for determining the value of the OCR-NOMA power allocation factor for effective spectrum sharing cooperation. Our analysis discovered significant ceiling effects, such as FRC, ESC, and SNC, that occur at higher target rates due to HIs. As a result, for building up a practical OCR-NOMA system, a reasonable limit on HIs level with a target rate can be calculated. We showed that FD CSAT is more resilient to HIs and outperforms benchmark PDLT over the entire SNR regime, as well as HD/OMA CSAT in the low SNR regime. DL was created as a new way for predicting system ESR with low computing cost and high accuracy. Numerical results revealed that the ergodic rate and ESR outcomes utilizing DNN prediction closely matched the Monte-Carlo simulation and analysis results. As a result, deploying a DNN as a black box might be considered as a new promising and effective technique to evaluating system performance through a low-latency estimation process that avoids the derivation of complicated closed-form equations in real-world network situations.

For future work, a possible extension of our work can incorporate an extended system model by deploying multiple antennas at the nodes and by exploring IRS with appropriate phase adjustment schemes. Albeit, with the Nakagami-*m* fading channels, the system performance measures require new formulations and pose different mathematical challenges for their analyses.

[4]We have chosen hidden layers experimentally and found that the used number of neurons are the parameters which are giving best results. We tried with various values of neurons and hidden layers but the used parameters are utilized and tested with state-of-the-art methods.

Appendix A
Proof of Theorem 1

The CDF $F_{\gamma_{sr}^{\mathrm{DT}}}(v)$ can be expressed using (6) as

$$F_{\gamma_{sr}^{\mathrm{DT}}}(v) = \mathbb{P}_r\left[|\hat{h}_{sr}|^2 < \frac{v(\Delta_r|h_{rr}|^2(1+\theta_{rr}^2)+\phi_{sr})}{\Delta_s(1-\theta_{sr}^2 v)}\right] = \int_0^{\infty}\left(\int_0^{\mathcal{L}(y)} f_{|\hat{h}_{sr}|^2}(x)\,dx\right) f_{|h_{rr}|^2}(y)\,dy, \quad (76)$$

where $\mathcal{L}(y) = \frac{v(\Delta_r y(1+\theta_{rr}^2)+\phi_{sr})}{\Delta_s(1-\theta_{sr}^2 v)}$. With $v < \frac{1}{\theta_{sr}^2}$, invoking the expression of PDF $f_{|\hat{h}_{sr}|^2}(x)$ and simplifying further using [34, eq. 3.351.1] and [34, eq. 1.111], (76) can be computed as $F_{\gamma_{sr}^{\mathrm{DT}}}(v) = \mathbb{J}_1(v) - \mathbb{J}_2(v)$. Subsequently, $\mathbb{J}_1(v) = \int_0^{\infty} f_{|h_{rr}|^2}(y)dy = 1$ and $\mathbb{J}_2(v)$ can be quantified as

$$\mathbb{J}_2(v) = \mathbb{J}_3 \int_0^{\infty} y^{(b+m_{rr}-1)} e^{-\left(\frac{m_{sr}v(1+\theta_{rr}^2)}{\hat{\Omega}_{sr}\Delta_s(1-\theta_{sr}^2 v)} + \frac{m_{rr}}{\Omega_{rr}\Delta_r}\right)y} dy, \quad (77)$$

with

$$\mathbb{J}_3 = \sum_{a=0}^{m_{sr}-1}\sum_{b=0}^{a} \frac{1}{a!}\frac{1}{\Gamma(m_{rr})}\left(\frac{m_{rr}}{\Omega_{rr}\,\Delta_r}\right)^{m_{rr}} \binom{a}{b} (\phi_{sr})^{a-b} \times (1+\theta_{rr}^2)^b \left(\frac{m_{sr}v}{\hat{\Omega}_{sr}\Delta_s(1-\theta_{sr}^2 v)}\right)^a e^{-\left(\frac{m_{sr}v\phi_{sr}}{\hat{\Omega}_{sr}\Delta_s(1-\theta_{sr}^2 v)}\right)}. \quad (78)$$

On solving the integral in (77) using [34, eq. 3.351.3] and simplifying further, one can get the required result in (14).

Appendix B
Proof of Theorem 2

With $\mathcal{P}_{u_2} = \mathbb{P}_r\left[\gamma_{su_2}^{\mathrm{DT}} \geq \tau_p - \gamma_{ru_2,x_s}^{\mathrm{DF}}, \gamma_{ru_2}^{\mathrm{DF}} \geq \tau_s\right]$, on inserting the corresponding SNDR expressions from (4), (9) and (10) and fetching the condition on $|\hat{h}_{ru_2}|^2$, we can analyze for $\tau_p > \gamma_{ru_2,x_s}^{\mathrm{DF}}$ and $\tau_p < \gamma_{ru_2,x_s}^{\mathrm{DF}}$, and obtain the expression in (29). Herein, the $\mathcal{P}_{u_{21}} = 1 - \mathbb{P}_r[\gamma_{su_2}^{\mathrm{DT}} < \tau_p - \gamma_{ru_2,x_s}^{\mathrm{DF}}]$ can be evaluated using H-stairways conjecture to obtain the result in (30). While, the $\mathcal{P}_{u_{22}} = \mathbb{P}_r\left[\gamma_{ru_2}^{\mathrm{DF}} \geq \tau_s\right] = 1 - F_{\gamma_{ru_2}^{\mathrm{DF}}}(x)$ can be evaluated for $\mathcal{T}_1 > 0$ as

$$\mathcal{P}_{u_{22}} = \int_{\frac{\mathcal{T}_2}{\mathcal{T}_1}}^{\infty}\left(\int_0^{\mathcal{T}_1 y - \mathcal{T}_2} f_{|h_{u_2}|^2}(x)\,dx\right) f_{|\hat{h}_{ru_2}|^2}(y)\,dy. \quad (79)$$

On substituting the expression of PDF $f_{|h_{u_2}|^2}(x)$ and solving the inner integral using [34, eq. 3.351.1] and [34, eq. 1.111], (79) can be simplified as $\mathcal{P}_{u_{22}} = \mathbb{A}_1(\tau_s) - \mathbb{A}_2(\tau_s)$, where

$$\mathbb{A}_1(\tau_s) = \int_{\frac{\mathcal{T}_2}{\mathcal{T}_1}}^{\infty} f_{|\hat{h}_{ru_2}|^2}(y)\, dy, \tag{80}$$

$$\mathbb{A}_2(\tau_s) = \sum_{a=0}^{m_{u_2}-1} \sum_{b=0}^{a} \binom{a}{b} \frac{1}{a!} (\mathcal{T}_1)^b (-\mathcal{T}_2)^{a-b} \left(\frac{m_{u_2}}{k_2 \Omega_{u_2}}\right)^a \times e^{\left(\frac{m_{u_2}\mathcal{T}_2}{k_2\Omega_{u_2}}\right)} \int_{\frac{\mathcal{T}_2}{\mathcal{T}_1}}^{\infty} y^b e^{-\left(\frac{m_{u_2}\mathcal{T}_1}{k_2\Omega_{u_2}}\right)y} f_{|\hat{h}_{ru_2}|^2}(y)\, dy. \tag{81}$$

Thus, on invoking the expression of PDF $f_{|\hat{h}_{ru_2}|^2}(y)$ and solving the associated integral with the help of [34, eq. 3.351.2], we obtain the results as presented in (32) and (33).

Appendix C
Proof of Theorem 3

To calculate R_{e,U_1} using (53), we first determine the CDF of X as

$$\begin{aligned} F_X(x) &= \mathbb{P}_r\big[\min\{(\gamma_{sr}^{\text{DT}}, \gamma_{u_1}^{\text{MRC}}, \gamma_{u_2}^{\text{MRC}}) \le x\}\big] \\ &= 1 - \big(\mathbb{P}_r\big[\gamma_{sr}^{\text{DT}} > x\big] \times \mathbb{P}_r\big[\gamma_{u_1}^{\text{MRC}} > x\big] \times \mathbb{P}_r\big[\gamma_{u_2}^{\text{MRC}} > x\big]\big) \\ &\triangleq 1 - \big(\mathbb{B}_1 \times \mathbb{B}_2 \times \mathbb{B}_3\big). \end{aligned} \tag{82}$$

Hereby, $\mathbb{B}_1$ is calculated as

$$\mathbb{B}_1 = \mathbb{P}_r\big[\gamma_{sr}^{\text{DT}} > x\big] = 1 - \mathbb{P}_r\big[\gamma_{sr}^{\text{DT}} \le x\big] = 1 - F_{\gamma_{sr}^{\text{DT}}}(x). \tag{83}$$

On invoking the CDF expression of $F_{\gamma_{sr}^{\text{DT}}}(x)$ from (14) into (83), we obtain $\mathbb{B}_1$ as

$$\begin{aligned} \mathbb{B}_1 = &\sum_{a=0}^{m_{sr}-1} \sum_{b=0}^{a} \frac{1}{a!} \left(\frac{m_{sr}\tau_p}{\hat{\Omega}_{sr}\Delta_s\vartheta}\right)^a \frac{1}{\Gamma(m_{rr})} \\ &\times \left(\frac{m_{rr}}{\Omega_{rr}\Delta_r}\right)^{m_{rr}} \binom{a}{b} (\phi_{sr})^{a-b} (1+\theta_{rr}^2)^b (b+m_{rr}-1)! \\ &\times \left(\frac{m_{sr}\tau_p(1+\theta_{rr}^2)}{\hat{\Omega}_{sr}\Delta_s\vartheta} + \frac{m_{rr}}{\Omega_{rr}\Delta_r}\right)^{-(b+m_{rr})} e^{-\left(\frac{m_{sr}\phi_{sr}\tau_p}{\hat{\Omega}_{sr}\Delta_s\vartheta}\right)}. \end{aligned} \tag{84}$$

Now, $\mathbb{B}_2$ can be obtained as

$$\mathbb{B}_2 = \mathbb{P}_r\big[\gamma_{u_1}^{\text{MRC}} > x\big] = 1 - \mathbb{P}_r\big[\gamma_{u_1}^{\text{MRC}} \le x\big] = 1 - \mathcal{P}_{u_1}. \tag{85}$$

On inserting $\mathcal{P}_{u_1}$ from (19) into (85), we obtain $\mathbb{B}_2$ as

$$\begin{aligned} \mathbb{B}_2 = 1 - &\sum_{i=0}^{H-1} \left\{ F_{\gamma_{su_1}^{\text{DT}}}\Big(\frac{i+1}{H}\,\tau_p\Big) - F_{\gamma_{su_1}^{\text{DT}}}\Big(\frac{i}{H}\,\tau_p\Big) \right\} \\ &\times F_{\gamma_{ru_1}^{\text{DF}}}\Big(\frac{H-i}{H}\,\tau_p\Big). \end{aligned} \tag{86}$$

Similarly, $\mathbb{B}_3$ can also be calculated as

$$\begin{aligned} \mathbb{B}_3 &= \mathbb{P}_r\big[\gamma_{u_2}^{\text{MRC}} > x\big] \\ &= 1 - \sum_{i=0}^{H-1} \left\{ F_{\gamma_{su_2}^{\text{DT}}}\Big(\frac{i+1}{H}\,\tau_p\Big) - F_{\gamma_{su_2}^{\text{DT}}}\Big(\frac{i}{H}\,\tau_p\Big) \right\} \\ &\quad \times F_{\gamma_{ru_2,x_s}^{\text{DF}}}\Big(\frac{H-i}{H}\,\tau_p\Big). \end{aligned} \tag{87}$$

Finally, on inserting $\mathbb{B}_1$, $\mathbb{B}_2$, and $\mathbb{B}_3$, from (84), (86) and (87) into (82) and then putting (82) into (53), it is realized that a closed-form solution for R_{e,U_1} could be intractable. Hence, we employ a Gaussian-Chebyshev quadrature [44] to find an approximation for the integral term in (53). With the Gaussian-Chebyshev quadrature method, the basic approximation relation is as follows:

$$\int_{-1}^{1} \frac{f(x)}{\sqrt{(1-x^2)}}\, dx \approx \frac{\pi}{N} \sum_{n=1}^{N} f\left[\cos\left(\frac{(2n-1)\pi}{2N}\right)\right]. \tag{88}$$

Now, on inserting $x = \frac{1+\Phi_n}{1-\Phi_n}$ into (53) and using (88), one can get the required result in (54), where $\Phi_n = \cos\left(\frac{(2n-1)\pi}{2N}\right)$ and N is a parameter to ensure a complexity-accuracy trade-off.

References

[1] S. K. Sharma, T. E. Bogale, L. B. Le, S. Chatzinotas, X. Wang, and B. Ottersten, "Dynamic spectrum sharing in 5G wireless networks with full-duplex technology: Recent advances and research challenges," *IEEE Commun. Surveys Tuts.*, vol. 20, no. 1, pp. 674-707, 1st Quart., 2018.

[2] L. Dai, B. Wang, Z. Ding, Z. Wang, S. Chen, and L. Hanzo, "A survey of non-orthogonal multiple access for 5G," *IEEE Commun. Surveys Tutorials*, vol. 20, no. 3, pp. 2294-2323, 2018.

[3] P. Wang, J. Xiao, and L. Ping, "Comparison of orthogonal and non-orthogonal approaches to future wireless cellular systems," *IEEE Veh. Technol. Mag.*, vol. 1, no. 3, pp. 4-11, 2006.

[4] R. V. Prasad, P. Pawelczak, J. A. Hoffmeyer, and H. S. Berger, "Cognitive functionality in next generation wireless networks: Standardization efforts," *IEEE Commun. Mag.*, vol. 46, no. 4, pp. 72-78, Apr. 2008.

[5] A. T. Hoang, Y. Liang, D. T. C. Wong, Y. Zeng, and R. Zhang, "Opportunistic spectrum access for energy-constrained cognitive radios," *IEEE Trans. Wireless Commun.*, vol. 8, no. 3, pp. 1206-1211, Mar. 2009.

[6] Y. Chen, J. Zhang, W. Feng, and M. -S. Alouini, "Radio sensing using 5G signals: Concepts, state of the art, and challenges," *IEEE Internet Things J.*, vol. 9, no. 2, pp. 1037-1052, Jan. 2022.

[7] V. Aswathi and A. V. Babu, "Performance analysis of NOMA-based underlay cognitive radio networks with partial relay selection," *IEEE Trans. Veh. Technol.*, vol. 70, no. 5, pp. 4615-4630, May 2021.

[8] G. Li, D. Mishra, and H. Jiang, "Channel-aware power allocation and decoding order in overlay cognitive NOMA networks," *IEEE Trans. Veh. Technol.*, vol. 69, no. 6, pp. 6511-6524, Jun. 2020.

[9] M. Vaezi, G. A. A. Baduge, Y. Liu, A. Arafa, F. Fang, and Z. Ding, "Interplay between NOMA and other emerging technologies: A survey," *IEEE Trans. Cogn. Commun. Netw.*, vol. 5, no. 4, pp. 900-919, Dec. 2019.

[10] S. Arzykulov, G. Nauryzbayev, T. A. Tsiftsis, B. Maham, and M. Abdallah, "On the outage of underlay CR-NOMA networks with detect-and-forward relaying," *IEEE Trans. Cogn. Commun. Netw.*, vol. 5, no. 3, pp. 795-804, Sep. 2019.

[11] V. Kumar, Z. Ding, and M. F. Flanagan, "On the performance of downlink NOMA in underlay spectrum sharing," *IEEE Trans. Veh. Technol.*, vol. 70, no. 5, pp. 4523-4540, May 2021.

[12] A. H. Bastami, "NOMA-based spectrum leasing in cognitive radio network: Power optimization and performance analysis," *IEEE Trans. Commun.*, vol. 69, no. 7, pp. 4821-4831, Jul. 2021.

[13] V. Singh, P. K. Upadhyay, and M. Lin, "On the performance of NOMA assisted overlay multiuser cognitive satellite-terrestrial networks," *IEEE Wireless Commun. Lett.*, vol. 9, no. 5, pp. 638-642, May 2020.

[14] J. Men, J. Ge, and C. Zhang, "Performance analysis of nonorthogonal multiple access for relaying networks over Nakagami-*m* fading channels," *IEEE Trans. Veh. Technol.*, vol. 66, no. 2, pp. 1200-1208, Feb. 2017.

[15] V. Aswathi and B. A. V., "Outage and throughput analysis of full-duplex cooperative NOMA system with energy harvesting," *IEEE Trans. Veh. Technol.*, vol. 70, no. 11, pp. 11648-11664, Nov. 2021.

[16] S. Dhanasekaran and C. M, "Performance analysis of NOMA in full-duplex cooperative spectrum sharing systems," *IEEE Trans. Veh. Technol.*, vol. 71, no. 8, pp. 9095-9100, Aug. 2022.

[17] G. Liu, F. R. Yu, H. Ji, V. C. M. Leung, and X. Li, "In-band full-duplex relaying: A survey, research issues and challenges," *IEEE Commun. Surveys Tuts.*, vol. 17, no. 2, pp. 500-524, 2nd Quart., 2015.

[18] A. Koohian, H. Mehrpouyan, A. A. Nasir, S. Durrani, and S. D. Blostein, "Residual self-interference cancellation and data detection in full-duplex communication system," in *Proc. IEEE Int. Conf. Commun. (ICC)*, May 2017, pp. 1-6.

[19] E. Ahmed and A. M. Eltawil, "All-digital self-interference cancellation technique for full-duplex systems," *IEEE Trans. Wireless Commun.*, vol. 14, no. 7, pp. 3519-3532, Jul. 2015.

[20] X. Li, Z. Xie, Z. Chu, V. G. Menon, S. Mumtaz, and J. Zhang, "Exploiting benefits of IRS in wireless powered NOMA networks," *IEEE Trans. Green Commun. Netw.*, vol. 6, no. 1, pp. 175-186, Mar. 2022.

[21] H. Liu, G. Li, X. Li, Y. Liu, G. Huang, and Z. Ding, "Effective capacity analysis of STAR-RIS-assisted NOMA networks," *IEEE Wireless Commun. Lett.*, vol. 11, no. 9, pp. 1930-1934, Sep. 2022.

[22] H. Huang *et al*., "Deep learning for physical-layer 5G wireless techniques: Opportunities, challenges and solutions," *IEEE Wireless Commun.*, vol. 27, no. 1, pp. 214-222, Feb. 2020.

[23] T. -H. Vu, T. -V. Nguyen, and S. Kim, "Wireless powered cognitive NOMA-based IoT relay networks: Performance analysis and deep learning evaluation," *IEEE Internet Things J.*, vol. 9, no. 5, pp. 3913-3929, Mar. 2022.

[24] Z. Zhang, Y. Lu, Y. Huang, and P. Zhang, "Neural network-based relay selection in two-way SWIPT-enabled cognitive radio networks," *IEEE Trans. Veh. Technol.*, vol. 69, no. 6, pp. 6264-6274, Jun. 2020.

[25] G. Gui, H. Huang, Y. Song, and H. Sari, "Deep learning for an effective non-orthogonal multiple access scheme," *IEEE Trans. Veh. Technol.*, vol. 67, no. 9, pp. 8440-8450, Sep. 2018.

[26] H. Huang, Z. Li, B. Ai, G. Wang, and M. S. Obaidat, "Impact of hardware impairment on spectrum underlay cognitive multiple relays network," in *Proc. IEEE Int. Conf. Commun.*, Kuala Lumpur, Malaysia, May 2016, pp. 1-6.

[27] S. Solanki, V. Singh, and P. K. Upadhyay, "RF energy harvesting in hybrid two-way relaying systems with hardware impairments," *IEEE Trans. Veh. Technol.*, vol. 68, no. 12, pp. 11792-11805, Dec. 2019.

[28] C. Deng, M. Liu, X. Li, and Y. Liu, "Hardware impairments aware full-duplex NOMA networks over Rician fading channels," *IEEE Syst. J.*, vol. 15, no. 2, pp. 2515-2518, Jun. 2021.

[29] V. Aswathi and A. V. Babu, "Full/half duplex cooperative NOMA under imperfect successive interference cancellation and channel state estimation errors," *IEEE Access*, vol. 7, pp. 179961-179984, Dec. 2019.

[30] S. Solanki, P. K. Upadhyay, D. B. da Costa, P. S. Bithas, and A. G. Kanatas, "Performance analysis of cognitive relay networks with RF hardware impairments and CEEs in the presence of primary users' interference," *IEEE Trans. Cogn. Commun. Netw.*, vol. 4, no. 2, pp. 406-421, Jun. 2018.

[31] S. Singh and M. Bansal, "Performance analysis of NOMA-based AF cooperative overlay system with imperfect CSI and SIC," *IEEE Access*, vol. 9, pp. 40263-40273, Mar. 2021.

[32] T. -H. Vu, T. -V. Nguyen, D. B. da Costa, and S. Kim, "Performance analysis and deep learning design of underlay cognitive NOMA-based CDRT networks with imperfect SIC and co-channel interference," *IEEE Trans. Commun.*, vol. 69, no. 12, pp. 8159-8174, Dec. 2021.

[33] V. Singh and P. K. Upadhyay, "Exploiting FD/HD cooperative NOMA in underlay cognitive hybrid satellite-terrestrial networks," *IEEE Trans. Cogn. Commun. Netw.*, vol. 8, no. 1, pp. 246-262, Mar. 2022.

[34] I. S. Gradshteyn and I. M. Ryzhik, *Tables of Integrals, Series and Products*, 6th ed. New York: Academic Press, 2000.

[35] T. Riihonen, S. Werner, and R. Wichman, "Hybrid full-duplex/half-duplex relaying with transmit power adaptation," *IEEE Trans. Wireless Commun.*, vol. 10, no. 9, pp. 3074-3085, Sep. 2011.

[36] *8 Hints for Making and Interpreting EVM Measurements*, Tech. Rep., Agilent Technologies, Santa Clara, CA, USA, 2005.

[37] X. Li, J. Li, Y. Liu, Z. Ding, and A. Nallanathan, "Residual transceiver hardware impairments on cooperative NOMA networks," *IEEE Trans. Wireless Commun.*, vol. 19, no. 1, pp. 680-695, Jan. 2020.

[38] X. Yue, Y. Liu, S. Kang, A. Nallanathan, and Z. Ding, "Exploiting full/half-duplex user relaying in NOMA systems," *IEEE Trans. Commun.*, vol. 66, no. 2, pp. 560-575, Feb. 2018.

[39] M. F. Kader, M. B. Shahab, and S. Y. Shin, "Exploiting non-orthogonal multiple access in cooperative relay sharing," *IEEE Commun. Lett.*, vol. 21, no. 5, pp. 1159-1162, May 2017.

[40] C. Zhang, J. Ge, J. Li, Y. Rui, and M. Guizani, "A unified approach for calculating outage performance of two-way AF relaying over fading channels," *IEEE Trans. Veh. Technol.*, vol. 64, no. 3, pp. 1218-1229, Mar. 2015.

[41] C. Guo, L. Zhao, C. Feng, Z. Ding, and H.-H. Chen, "Energy harvesting enabled NOMA systems with full-duplex relaying," *IEEE Trans. Veh. Technol.*, vol. 68, no. 7, pp. 7179-7183, Jul. 2019.

[42] C. Nwankpa, W. Ijomah, A. Gachagan, and S. Marshall, "Activation functions: Comparison of trends in practice and research for deep learning," 2018, *arXiv:1811.03378.*, [Online]. Available: http://arxiv.org/abs/1811.03378

[43] T. Dozat, "Incorporating Nesterov momentum into Adam," in Proc. *ICLR*, Feb. 2016, pp. 1-4.

[44] M. Abramowitz and I. Stegun, *Handbook of Mathematical Functions With Formulas, Graphs, and Mathematical Tables,* 10th ed. New York, NY, USA: Dover, 1972.

Chandan Kumar Singh (Student Member, IEEE) received the B.Tech. degree in Electronics and Communication Engineering from Maulana Abul Kalam Azad University of Technology, West Bengal (Kolkata), India, in 2011 and the M.Tech. degree in Digital Communication from the Netaji Subhas University of Technology (East Campus), Govt. of NCT of Delhi, India, in 2017. He is currently working toward the Ph.D. degree in Electrical Engineering, Indian Institute of Technology Indore, Madhya Pradesh, India. His research interests include next generation wireless communication, NOMA technique, cognitive radio, cooperative relaying, energy harvesting, physical layer security and mmWave.

Prabhat Kumar Upadhyay (Senior Member, IEEE) received the Ph.D. degree in Electrical Engineering from the Indian Institute of Technology (IIT) Delhi, New Delhi, India, in 2011. He joined IIT Indore in 2012 as an Assistant Professor in the Department of Electrical Engineering, where he became Associate Professor in 2017 and a Professor in 2022. He was a Visiting Professor at the Centre for Wireless Communications (CWC), University of Oulu, Finland during May-August 2022 under Nokia Foundation Fellowship. His general research interests include wireless and mobile communications, Internet of Things (IoT) networks, molecular communications and nano-networks.

Prof. Upadhyay is currently serving as an Editor for IEEE Transactions on Vehicular Technology and IEEE Communications Letters. He served as a Guest Editor of the Special Issue on "Energy-Harvesting Cognitive Radio Networks" in the IEEE Transactions on Cognitive Communications & Networking in 2018, and as an Associate Editor for IEEE Access during Jan. 2018 - Jan. 2022. He has also been involved in the Technical Program Committee of several IEEE premier conferences. He received the Exemplary Editor Award of the IEEE Communications Letters, 2021. He has been awarded the Sir Visvesvaraya Young Faculty Research Fellowship under the Ministry of Electronics and Information Technology (MeitY), Government of India, 2018-2023. He has been conferred with IETE- N V Gadadhar Memorial Award, 2022 and IETE-Prof SVC Aiya Memorial Award, 2018. He has co-authored a paper that received the Best Poster Award in COMSNETS, Bengaluru, 2023 and a paper that received the Best Paper Award in the CommNet, Morocco, 2018. He is a Fellow of the IETE and Fellow of the Institution of Engineers (India).

Janne J. Lehtomäki (Member, IEEE) received the Doctorate degree from the University of Oulu, Finland, in 2005. Currently, he is an Adjunct Professor at the Centre for Wireless Communications, University of Oulu. In Fall 2013, he spent the semester at Georgia Tech, Atlanta, USA, as a Visiting Scholar. He is also focusing on spectrum measurements and terahertz band wireless communications. He is also an Editorial Board Member of Physical Communication. He has coauthored the paper receiving the Best Paper Award in IEEE WCNC 2012. He was the General Co-Chair of IEEE WCNC 2017 International Workshop on Smart Spectrum, the TPC Co-Chair for IEEE WCNC 2015 and 2016 International Workshop on Smart Spectrum, and the Publicity/Publications Co-Chair for ACM NANOCOM 2015, 2016, and 2017. He has served as a Guest Associate Editor for the IEICE Transactions on Communications Special Section (February 2014 and July 2017) and as a Managing Guest Editor for Nano Communication Networks Special Issue (June 2016).